An ortholog of *P. falciparum* chloroquine resistance transporter (PfCRT) plays a key role in maintaining the integrity of the endolysosomal system in *Toxoplasma gondii* to facilitate host invasion

L. Brock Thornton[1], Paige Teehan[1#a], Katherine Floyd[1¶], Christian Cochrane[1¶], Amy Bergmann[1¶], Bryce Riegel[2], Paul D. Roepe[2] and Zhicheng Dou[1*]

1. Dept. of Biological Sciences, Clemson University, Clemson, South Carolina, 29634, United States of America

2. Depts. of Chemistry and of Biochemistry and Cellular and Molecular Biology, Georgetown University, 37th and O Streets NW, Washington DC 20057, United States of America

[#a]Current Address: Department of Biochemistry and Molecular Biology, The Pennsylvania State University, Pennsylvania, United States of America

*Corresponding author

E-mail: zdou@clemson.edu (ZD)

¶These authors contributed equally to this work.

Short title: Dynamics of the digestive vacuole in *Toxoplasma gondii*

Abstract

Toxoplasma gondii is an apicomplexan parasite with the ability to use foodborne, zoonotic, and congenital routes of transmission that causes severe disease in immunocompromised patients. The parasites harbor a lysosome-like digestive vacuole, termed the "Vacuolar Compartment/Plant-Like Vacuole" (VAC/PLV), which plays an important role in maintaining the lytic cycle and virulence of *T. gondii*. The VAC supplies proteolytic enzymes that are required to mature the parasite's invasion effectors and that digest autophagosomes and endocytosed host proteins. Previous work identified a *T. gondii* ortholog of the *Plasmodium falciparum* chloroquine resistance transporter (PfCRT) that localized to the VAC. Here, we show that TgCRT is a membrane transporter that is functionally similar to PfCRT. We also genetically ablate *TgCRT* and reveal that TgCRT protein plays a key role in maintaining the integrity of the parasite's endolysosomal system by controlling morphology of the VAC. When TgCRT is absent, the VAC dramatically increases in size by ~15-fold and co-localizes with its adjacent endosome-like compartment. Presumably to reduce aberrant swelling, transcription and translation of endolysosomal proteases are decreased in Δ*TgCRT* parasites. Expression of one endolysosomal subtilisin protease is quite significantly reduced, which impedes trimming of micronemal proteins, and significantly decreases parasite invasion. Chemical and genetic inhibition of proteolysis within the VAC reverses these effects, reducing VAC size and partially restoring the endolysosomal system, micronemal protein trimming, and invasion. Taken together, these findings reveal for the first time a physiological role of TgCRT in controlling VAC volume and the integrity of the endolysosomal system in *T. gondii*.

Author Summary

Toxoplasma gondii is an obligate intracellular protozoan parasite that belongs to the phylum Apicomplexa and that infects virtually all warm-blooded organisms. Approximately one-third of the human population is infected with *Toxoplasma*. The parasites invade host cells via processed invasion effectors in order to disseminate infection. A lysosome-like digestive vacuole (VAC) is involved in refining these invasion effectors to reach their final forms. A *T. gondii* ortholog of the malarial chloroquine resistance transporter protein (TgCRT) was found to be localized to the VAC membrane. Although the mutated version of the malarial chloroquine resistance transporter (PfCRT) has been shown to confer resistance to chloroquine treatment, its physiologic function remains poorly understood. Comparison between the related PfCRT and TgCRT proteins facilitates definition of the physiologic role of CRT proteins. In this study, we report that TgCRT plays a key role in regulating the integrity and proteolytic activity of the VAC and adjacent organelles, the secretion of invasion effectors, and parasite invasion and virulence. To relieve osmotic stress caused by VAC swelling when TgCRT is deleted, parasites repress proteolytic activities within this organelle to decrease solute accumulation, which then has secondary effects on parasite invasion. Our findings highlight a common function for PfCRT and TgCRT proteins in regulating apicomplexan parasite vacuolar size and function.

59 **Introduction**

60 *Toxoplasma gondii* uses polypeptide invasion factors to efficiently invade host cells. These proteins
61 are stored in two unique organelles in *Toxoplasma* parasites, the microneme and rhoptry. The micronemal
62 proteins undergo a series of proteolytic cleavage steps within the parasite's endosomal system, followed
63 by further intramembrane cleavage and trimming on the parasite's cell membrane before secretion [1,2].
64 Proper maturation and secretion of micronemal proteins are crucial for efficient invasion of parasites [3-5].
65

66 Micronemal protein maturation is regulated by several proteases. During intracellular trafficking, the
67 micronemal proteins are first cleaved by aspartyl protease 3 (TgASP3) in a post-Golgi compartment [5]. A
68 cathepsin L-like protease (TgCPL) was also shown to process some micronemal proteins in the endosome-
69 like compartment (ELC) of the parasite [4]. The mature proteins then pass through the microneme and
70 undergo further intramembrane cleavage and trimming on the parasite's surface. A plasma membrane-
71 bound protease, rhomboid 4 (TgROM4), is required to process at least some micronemal proteins and to
72 release them from the cell surface. TgROM4 substrates include micronemal protein 2 (TgMIC2) and apical
73 membrane antigen (TgAMA1) [5-8]. Subsequently, a subtilisin ortholog, TgSUB1, was shown to proteolyze
74 some micronemal proteins into their final forms, including TgMIC2 and TgMIC2-associated protein
75 (TgM2AP) [3]. Overall, precise control of proteolytic activities within the parasite's endosomal system and
76 on the plasma membrane is critical for processing parasite invasion effectors.
77

78 Among these proteases, TgCPL and TgSUB1 are both localized to the parasite's endolysosomal
79 system. TgCPL is located in an acidic digestive vacuole, termed the Vacuolar Compartment/Plant-like
80 Vacuole (VAC) in *Toxoplasma* parasites [4,9]. Our previous studies showed that the genetic ablation of
81 *TgCPL* causes defects in parasite invasion and acute virulence [4,10]. TgCPL becomes activated in the
82 VAC and a portion of TgCPL is delivered to the juxtaposed ELC for maturation [4]. TgSUB1 is a micronemal
83 protease and contains a GPI anchor necessary for membrane association [3]. TgSUB1 was shown to be
84 activated in a post-ER compartment and to enter the parasite's endolysosomal system before trafficking
85 to the microneme [11]. The deletion of *TgSUB1* led to inefficient trimming of micronemal proteins on the

86 parasite surface, thereby leading to defects in invasion and virulence [3]. Hence, the maintenance of the
87 integrity of the parasites' endolysosomal system is critical to regulating the distribution and activity of
88 endolysosomal proteases.
89
90 In addition to VAC dysfunction resulting in reduced invasion, replication, and virulence [4,10], parasites
91 with impaired VAC function are unable to turn over autophagosomes during chronic infection and thereby
92 cannot survive in host brain tissue [12]. Despite its importance, the VAC has not been well-characterized.
93 Only 4 proteins have been localized to the VAC, including TgCPL, TgCPB (a cathepsin B-like protein),
94 TgCRT (a *Toxoplasma* ortholog of chloroquine resistance transporter), and TgVP1 (a pyrophosphatase)
95 [4,13-15]. The VAC forms an intact organelle during initial infection and subsequently fragments during
96 intracellular replication [4]. It is unknown how parasites regulate these and other morphological changes
97 that occur within the endolysosomal system. In a previous study, *TgCRT* expression was knocked down
98 in type I *Toxoplasma* parasites using a tetracycline-inducible system [14], and VAC swelling was observed,
99 suggesting that TgCRT is involved in VAC volume regulation. Fitness defects were also seen in these
100 parasites suggesting that proper VAC morphology is essential for invasion and / or growth.
101
102 Interestingly, the swollen VAC phenotype for *TgCRT* knockdowns mirrors the enlarged digestive
103 vacuole (DV) phenotype for chloroquine-resistant (CQR) *Plasmodium falciparum* expressing CQR-
104 associated mutant PfCRT [16]. More recently, a L272F PfCRT mutation, along with CQR-conferring
105 mutations, was found to increase DV volume by an additional 1 - 2 μm^3 [17]. *In vitro* assays using purified
106 recombinant PfCRT, reconstituted in proteoliposomes, suggest that PfCRT transports aminoquinoline
107 drugs, basic amino acids, and perhaps oligopeptides, likely in an electrochemically coupled fashion [18,19].
108 With respect to drug transport, PfCRT expressed within CQR *P. falciparum* appears to exhibit higher
109 chloroquine (CQ) transport efficiency relative to PfCRTs found in chloroquine-sensitive (CQS) strains [18-
110 20]. These findings suggest that the PfCRT regulates the transport of key osmolytes from the *P. falciparum*
111 DV. Unfortunately, the inability to successfully ablate the *PfCRT* gene [21] limits additional analysis of
112 function *in vivo*.

113

114 Here, we successfully delete the *TgCRT* gene in a Type I *Toxoplasma* parasite strain by double
115 crossover homologous recombination. The resulting mutant, Δ*crt,* displayed a severely swollen VAC and
116 arrested VAC-ELC co-localization. Surprisingly, this aberrant organellar organization reduces transcription
117 and translation of several proteases residing in the parasite's endolysosomal system, altering microneme
118 secretion and resulting in defective parasite invasion and acute virulence. We also engineer successful
119 overexpression of wild type TgCRT constructs in yeast and show that the protein mediates CQ transport.
120 Collectively, these findings determine a novel role for TgCRT in regulating VAC volume and maintaining
121 endolysosomal integrity, suggest functional similarities for TgCRT and PfCRT proteins, and provide a new
122 model system for analyzing the function of apicomplexan CRT proteins.

123

124 **Results**

125 **1. Deletion of *TgCRT* in *Toxoplasma gondii*.**

126 Previous studies have utilized an anhydrotetracycline-regulated system to reduce levels of expression
127 of *TgCRT* in a Type I *Toxoplasma* RH strain [14]. However, incomplete depletion of *TgCRT* limits further
128 characterization of its function. Here, we adopted a genetically tractable RH-derived strain, termed
129 RHΔ*ku80* (hereafter referred to as WT), to produce a complete *TgCRT* knockout. The RHΔ*ku80* strain
130 represses the non-homologous end-joining DNA repair pathway to facilitate homology dependent DNA
131 recombination [22]. Due to the increased homologous recombination efficiency, this strain has been widely
132 used as a wild type *Toxoplasma* strain. We PCR amplified ~1.5-kb regions of the 5'- and 3'-untranscribed
133 regions (UTRs) of *TgCRT*, and flanked both at both 5'- and 3'-ends with a bleomycin (*BLE*) resistance
134 cassette to assemble a *TgCRT* knockout plasmid. The resulting construct was transfected into WT
135 parasites to replace the entire *TgCRT* gene with a *BLE* resistance cassette by double crossover
136 homologous recombination (**Fig 1A**). PCR analysis was performed to test for proper integration and
137 detected the presence of the *BLE* cassette and the loss of *TgCRT* as shown in the scheme for the
138 generation of the *TgCRT* knockout in Fig 1A. Amplification of ~1.6 kb fragments at both the 5'- and 3'-end

139 integration regions (5'- and 3'-ARMs) were observed in the *TgCRT* knockout (Δ*crt*), and a ~1.5 kb *TgCRT*
140 coding region was also missing within Δ*crt* (**Fig 1B**).

141 To complement loss of *TgCRT*, we modified the pTub-TgCRT-mCherry-3xmyc plasmid (a kind gift from
142 Dr. Giel van Dooren), which over-expresses a mCherry-3xmyc epitope-tagged *TgCRT* under control of the
143 *Toxoplasma* tubulin promoter. A 1 kb DNA region containing the cognate *TgCRT* promoter was PCR-
144 amplified and used to replace the tubulin promoter to provide similar transcription of complemented versus
145 endogenous *TgCRT*. The same primer set used to detect loss of *TgCRT* in the Δ*crt* strain in Fig 1B was
146 used to confirm integration of exogenously introduced *TgCRT*. Since the complemented *TgCRT* gene lacks
147 introns, a ~0.2 kb PCR product was observed in the Δ*crtCRT* complementation strain, whereas a ~1.5 kb
148 fragment was found for the WT strain (**Fig 1C**). To confirm that transcription of *TgCRT* in the Δ*crtCRT*
149 strain was comparable to endogenous levels, SYBR® Green-based quantitative PCR (qPCR) was used to
150 quantify messenger *TgCRT* RNA in WT, Δ*crt*, and Δ*crtCRT* strains. No *TgCRT* transcripts were observed
151 in Δ*crt*, further validating successful gene disruption. *TgCRT* transcript levels were similar between the WT
152 and Δ*crtCRT* strains (**Fig 1D**). These data showed successful ablation of the *TgCRT* gene in *Toxoplasma*
153 parasites, and properly restored expression with exogenously introduced *TgCRT* for the Δ*crtCRT* strain.
154

155 **2. TgCRT-deficient parasites lose endolysosomal system integrity due to altered VAC morphology.**

156 Upon obtaining RHΔ*ku80*Δ*crt*, we observed that purified extracellular Δ*crt* parasites exhibited large
157 concave subcellular structures under differential interference contrast (DIC) microscopy, whereas WT and
158 Δ*crtCRT* strains did not display this phenotype (**Fig 1E**). This subcellular structure was also observed in
159 pulse invaded Δ*crt* parasites (**Fig 1F**). To identify the swollen structures, we stained the WT, Δ*crt*, and
160 Δ*crtCRT* parasites with anti-TgCPL antibodies. TgCPL is a major luminal endoprotease in the VAC of
161 *Toxoplasma* [4,23]. Immunofluorescence microscopy showed that TgCPL staining co-localized with
162 concave subcellular structures in Δ*crt* **(Fig 1F)**. The TgCPL staining in Δ*crt* was larger than in WT and
163 Δ*crtCRT* parasites, indicating that the VAC becomes swollen when TgCRT is absent. We quantified the
164 VAC sizes based on TgCPL staining as described previously [12,14]. VAC diameter for the Δ*crt* parasites
165 (1.12 ± 0.07 μm, mean ± standard deviation) is approximately 2.6-fold larger than for WT parasites (0.43

166 ± 0.03 μm), while for Δ*crtCRT* (0.46 ± 0.02 μm) VAC was similar to that measured for WT parasites **(Fig**
167 **1F**). If we assume the VAC is approximately spherical, then the Δ*crt* parasite VAC is approximately 15-fold
168 larger than the WT VAC (**Fig 1F**). In contrast to pulse invaded parasites, the swollen concave structure
169 was not observed in replicated Δ*crt* parasites (**Fig 1G**). However, TgCPL staining showed differences
170 between WT and Δ*crt* parasites (**Fig 1G**). For WT, VAC fragments that appear during replication appear
171 as fragmented puncta upon TgCPL staining [4]. However, TgCPL staining revealed a single punctate
172 structure in replicating Δ*crt* parasites (**Fig 1G**). Overall, we find that loss of TgCRT severely alters the
173 morphology of the VAC in growing as well as replicating *Toxoplasma*.
174
175 The VAC is a lysosome-like organelle, participating in the parasite's endolysosomal system. It provides
176 an environment for maturation of TgCPL and delivers activated TgCPL to its adjacent endosome-like
177 compartment (ELC) to assist in processing micronemal proteins required for parasite invasion [4]. It also
178 serves as a digestive vacuole to digest endocytosed proteins [4,10,24]. We hypothesized that the dramatic
179 swelling of the VAC might affect the integrity of the parasite's endolysosomal system. We stained WT, Δ*crt*,
180 and Δ*crtCRT* parasites with antibodies recognizing markers of the VAC (anti-TgCPL) and of the ELC (anti-
181 proTgM2AP or TgVP1) [4]. In pulse invaded parasites, the VAC and ELC displayed distinct subcellular
182 staining in WT and Δ*crtCRT* strains, whereas in Δ*crt* parasites both markers partially co-localized **(Fig 1G).**
183 Similarly, the single TgCPL punctum in replicating Δ*crt* parasites also showed partial co-localization with
184 both proTgM2AP and TgVP1 (**Fig 1G**). These findings suggest that TgCRT mediated VAC morphology
185 affects the integrity of the parasite's endolysosomal system.
186
187 **3. RHΔ*ku80*Δ*crt* shows reduced invasion and acute virulence.**
188 *Toxoplasma* utilizes exocytosis and endocytosis via the endolysosomes to release micronemal
189 invasion effectors, and to ingest host proteins required for intracellular growth, respectively [10,25-27]. We
190 therefore characterized invasion, replication, and egress for the RHΔ*ku80*Δ*crt* strain. First, we measured
191 the invasion efficiency of parasites at 30-120 min post-infection. At 30 min post-infection, the Δ*crt* mutant
192 showed ~50% reduction in invasion compared to WT and Δ*crtCRT* **(Fig 2A)**. The differences in invasion

193 efficiency between WT and Δ*crt* were reduced to ~20% at 60 min post-infection, and were not seen at 120
194 min post-infection **(Fig 2A)**, suggesting that Δ*crt* parasites have slower invasion kinetics relative to the WT
195 strain. Second, we used immunofluorescence microscopy to quantify parasite replication. Infected cells
196 were stained with DAPI and anti-TgGRA7 antibody to define individual parasite nuclei and parasitophorous
197 vacuolar (PV) membranes, respectively. The average number of parasites per PV was calculated for each
198 strain in order to compare replication rates. There were no statistical differences in parasite replication
199 between WT and Δ*crt* parasites at 28 and 40 hrs post-infection **(Fig 2B)**. We also introduced NanoLuc®
200 luciferase into WT, Δ*crt*, and Δ*crtCRT* parasites, and measured the fold-change in luciferase activity for 72
201 hrs post-infection in order to calculate relative growth rates. Similarly, we did not observe growth
202 differences between WT and Δ*crt* at 24, 48, and 72 hrs post-infection **(Fig 2B)**. Third, the egress efficiency
203 of each strain was determined by a lactate dehydrogenase release-based assay. The parasites were
204 incubated with 0.5 mM Zaprinast for 5 min to induce egress. The egressed parasites disrupt host cell
205 membranes to release lactate dehydrogenase that is subsequently quantified to extrapolate to the number
206 of egressed PVs. We did not observe egress defects in the *TgCRT*-deficient parasites **(Fig 2C)**. Last, we
207 determined the acute virulence of Δ*crt* parasites in a murine model. Outbred CD-1 mice were infected with
208 a subcutaneous or intravenous inoculum of 100 WT, Δ*crt*, or Δ*crtCRT* parasites. Thirty percent of mice
209 infected with the Δ*crt* mutant survived when mice were infected by subcutaneous injection, while the WT
210 and Δ*crtCRT* infections led to mortality at 10-12 days post-infection **(Fig 2D)**. Mice receiving WT parasites
211 by intravenous inoculation showed mortality starting at 13 days post-infection and all were expired at 20
212 days. The Δ*crt* and Δ*crtCRT* parasites caused death in 40% and 80% of infected mice respectively **(Fig**
213 **2D)**. Statistical analysis showed that mice infected with WT and Δ*crt* parasites have significantly different
214 survival. Seroconversion of the surviving mice was confirmed by ELISA (not shown). We also challenged
215 surviving Δ*crt* mice with 1000 WT parasites by subcutaneous injection, and did not observe lethality after
216 30 days post-challenge. These findings indicate that the pre-inoculation of Δ*crt* parasites conferred
217 immunological protection to subsequent acute toxoplasmosis. Collectively, our findings revealed that
218 *Toxoplasma* parasites require the TgCRT protein for optimal invasion and acute virulence but not for
219 replication and egress.

220

221 **4. RH∆*ku80*∆*crt* shows impaired microneme secretion.**

222 During infection, *Toxoplasma* parasites sequentially secrete proteins to facilitate host invasion.
223 Micronemal proteins are the first to be secreted. These traffic through the parasite's endolysosomal system
224 and undergo intracellular maturation, intramembrane cleavage, and cell surface trimming before secretion
225 [3-8,28]. To test which step(s) was (were) affected in the ∆*crt* parasites, we probed cell lysates and
226 excretory secretory antigen (ESAs) fractions of each strain with anti-TgMIC2, anti-TgM2AP, and anti-
227 TgMIC5 (antibodies to three representative micronemal proteins) by immunoblotting to measure
228 abundances and secretion patterns. The migration patterns of these three micronemal proteins in cell
229 lysates were very similar among the strains. The abundances of the individual micronemal proteins were
230 normalized against the protein level of *Toxoplasma* actin protein by densitometry and plotted for
231 quantification. All three strains showed comparable steady state abundances of these proteins **(Fig 3A)**.
232 To further evaluate abundances, we probed constitutive and induced ESAs with the same antibodies. The
233 constitutive and induced ESAs were generated by incubating purified parasites in D10 medium (DMEM
234 medium supplemented with 10% (v/v) cosmic calf serum) for 30 min at 37ºC or D10 medium supplemented
235 with 1% (v/v) ethanol for 2 min at 37ºC, respectively. In the ESAs secreted by WT parasites, TgMIC2
236 exhibited two bands migrating at 100 kDa and 95 kDa, while TgM2AP showed 4 proteolytically processed
237 polypeptides along with pro- and mature forms. However, TgMIC2 only existed as a 100 kDa band in ∆*crt*
238 parasites. Furthermore, mature TgM2AP was not processed in the constitutive ESAs of the ∆*crt* strain and
239 showed significantly reduced processing in the induced ESAs of ∆*crt* parasites **(Fig 3B)**. The secreted
240 TgMIC5 protein displayed similar migration patterns among these strains **(Fig 3B)**. Secretion of these
241 micronemal proteins was also quantified by normalizing the relative abundances of the proteins against
242 the protein level of secreted TgGRA7, a dense granule protein. The secretion of TgMIC2, TgM2AP, and
243 TgMIC5 were reduced by ~80%, 35%, and 40%, respectively, in the induced ESAs of ∆*crt* parasites,
244 compared to the WT strain. The differences in the amount of microneme secretion were less significant in
245 the constitutive ESAs. Only TgMIC2 secretion was decreased by ~55% in ∆*crt* parasites compared to the
246 WT strain, while TgM2AP and TgMIC5 did not show differences **(Fig 3B)**. To examine whether the

247 abnormal secretion of micronemal proteins alters their intracellular trafficking patterns, we stained pulse
248 invaded and replicated parasites with TgMIC2 and TgM2AP antibodies. Both microneme proteins trafficked
249 to the apical end of the parasites and showed normal staining patterns (**Fig 3C**).
250
251 Prior to secretion, some membrane-anchored micronemal proteins are released via proteolytic
252 cleavage by intramembrane rhomboid proteases such as TgROM4. The deletion of TgROM4 leads to
253 retention of some micronemal proteins on the parasite's plasma membrane, such as TgMIC2 and TgAMA1
254 (*Toxoplasma* apical membrane antigen 1) [6-8,28]. To test whether the aberrant endolysosomal system
255 alters the retention of micronemal proteins on the surface of parasites, we stained the purified, non-
256 permeabilized extracellular parasites with anti-TgMIC2 antibody. Immunofluorescence microscopy did not
257 reveal excess TgMIC2 on the plasma membrane of Δ*crt* parasites **(Fig S1)**, suggesting that the reduced
258 secretion of micronemal proteins is not due to inefficient intramembrane cleavage of micronemal proteins
259 on the parasite's plasma membrane.
260
261 The endosome-like compartment is involved not only in the trafficking of micronemal proteins, but also
262 rhoptry contents [29]. We stained newly invaded and replicated parasites with anti-TgROP7 antibodies to
263 examine the trafficking of rhoptry proteins and the morphology of the rhoptry. The TgROP7 staining
264 revealed typical rhoptry patterns located at the apical end of the parasites (**Fig 3D**), excluding the possibility
265 of aberrant trafficking of rhoptry contents and possible defects in biogenesis. Taken together, our data
266 suggest that invasion defects for Δ*crt* parasites are caused by incomplete trimming and consequent
267 inefficient secretion of micronemal proteins, but not by altered intracellular maturation, trafficking, or
268 intramembrane cleavage of micronemal proteins, nor by altered rhoptry morphology.
269
270 **5. TgSUB1 transcript and protein levels are decreased for Δ*crt* parasites.**
271 The inefficient proteolytic processing of TgMIC2 and TgM2AP in RHΔ*ku80*Δ*crt* ESAs led us to
272 investigate the abundance of *Toxoplasma* subtilisin 1 (TgSUB1) in the Δ*crt* parasites. A previous
273 publication reported that parasites lacking TgSUB1 showed defective trimming patterns for secreted

274 micronemal proteins, such as TgMIC2 and TgM2AP [3], which seemed, to us, to be similar to the secretion
275 patterns observed for the Δ*crt* mutant. Therefore, we quantified secreted TgSUB1 in both constitutive and
276 induced ESAs by probing them with an anti-SUB1 antibody, previously found to specifically react against
277 TgSUB1 and PfSUB1 [30]. Immunoblotting analysis revealed that there was no detectable TgSUB1 in the
278 ESAs of Δ*crt* parasites **(Fig 4A).** Non-permeabilized extracellular parasites were also stained with anti-
279 SUB1 to evaluate the amount of surface-anchored TgSUB1. Similarly, there was no detectable TgSUB1
280 staining on the plasma membrane of Δ*crt* parasites (**Fig 4B**). These data suggest that TgSUB1 is not
281 efficiently delivered to the surface of parasites in the Δ*crt* mutant.
282
283 TgSUB1 is a micronemal protein that also traffics through the parasite's endolysosomal system [3,11].
284 The aberrant endolysosomal system in Δ*crt* parasites potentially alters intracellular trafficking and/or
285 maturation of TgSUB1 that then reduces expression. To test these possibilities, first, we stained pulse
286 invaded and replicated parasites with anti-SUB1 to examine TgSUB1 intracellular trafficking patterns.
287 TgMIC5 localization was used as a reference for typical expected microneme staining. Surprisingly, we
288 observed much less TgSUB1 staining in Δ*crt* parasites compared to the WT strain (**Fig 4C**). Next, we
289 quantified abundance of TgSUB1 in parasite cell lysates and found that TgSUB1 was decreased by
290 approximately 90% in Δ*crt* parasites compared to WT parasites **(Fig 4D)**. To further understand how
291 TgSUB1 expression is suppressed in the Δ*crt* mutant, we performed qPCR to measure *TgSUB1* mRNA
292 for WT, Δ*crt*, and Δ*crtCRT* parasites. *TgSUB1* transcript was reduced ~10-fold upon deletion of *TgCRT*
293 **(Fig 4E)**. Collectively, our findings suggest that arrested co-localization of the VAC and ELC dramatically
294 decreases the abundance of TgSUB1 protein, which then alters the proteolytic processing of normally
295 secreted micronemal protein invasion effectors, thereby reducing invasion efficiency.
296
297 **6. VAC alterations reduce endolysosomal protease proteins and transcripts.**
298 The swollen VAC and its aberrant co-localization with the ELC in the Δ*crt* parasites could conceivably
299 lead to altered gene transcription to assist in the adaptation of these parasites. We conducted
300 transcriptome sequencing to detect global alterations in gene transcription for Δ*crt* parasites relative to WT.

301 The differential gene expression analysis identified 102 genes whose transcript levels changed greater
302 than 1.5-fold in the Δ*crt* strain. Forty-six and fifty-six genes had increased and reduced transcripts,
303 respectively (**Fig 5A and Table S1**).
304
305 Four proteases were among the list of genes showing reduced transcripts in the Δ*crt* mutant, including
306 one putative aminopeptidase N protein (TgAMN, TGGT1_221310), one putative Pro-Xaa serine
307 carboxypeptidase (TgSCP, TGGT1_254010), aspartyl protease 1 (TgASP1, TGGT1_201840), and an ICE
308 family protease-like protein (TgICEL, TGGT1_243298). We validated transcript levels for these proteases,
309 as well as two known VAC luminal proteases (TgCPL and TgCPB), in WT, Δ*crt*, and Δ*crtCRT* strains by
310 qPCR. The qPCR analysis showed that the transcript levels of TgAMN, TgSCP, TgASP1, and TgCPB
311 were decreased by 50%, 20%, 47%, and 14%, respectively, in Δ*crt* parasites **(Fig 5B)**. Protein levels of
312 TgCPL and TgCPB were quantified by immunoblotting and compared for WT, Δ*crt*, and Δ*crtCRT* parasites.
313 Although TgCPL transcript levels did not differ, abundance of TgCPL protein was decreased ~25% in the
314 Δ*crt* mutant **(Fig 5C)**. *TgCPB* expression was reduced and both the pro- and mature forms of TgCPB
315 protein were reduced relative to WT parasites. **(Fig 5C)**.
316
317 To determine the subcellular locations of these down-regulated proteases, we tagged endogenous
318 TgAMN and TgSCP with 3xHA and 3xmyc epitope tags at their C-termini in WT parasites, respectively
319 **(Fig S2)**. After drug-selection, we probed cell lysates from these tagged strains with anti-HA and anti-myc
320 antibodies, respectively, to test expression. Immunoblotting revealed that the observed molecular mass of
321 both proteins was similar to the predicted size based on primary sequences (**Fig 5D**). Next, the tagged
322 strains were co-stained with antibodies recognizing the epitope tags along with anti-TgCPL and anti-VP1
323 antibodies to determine subcellular location. Immunofluorescence microscopy revealed both TgSCP and
324 TgAMN to be in the VAC/ELC (**Fig 5D**) TgASP1 subcellular location was also determined to be within the
325 VAC (data not shown; Dou, Z. *et al*., in preparation). Collectively, these data suggest that the swollen VAC
326 in Δ*crt* parasites causes reduced transcription and translation of several endolysosomal proteases.
327

328 **7. Suppression of proteolysis within the swollen Δ*crt* VAC partially restores VAC size, organellar**
329 **separation, and invasion.**

330 We suspected that inhibition of proteolysis might reduce the size of the swelled VAC. We tested this
331 hypothesis by chemically and genetically suppressing VAC proteolysis. First, we treated WT, Δ*crt*, and
332 Δ*crtCRT* parasites with 1 μM LHVS, an irreversible inhibitor of TgCPL protease [23]. As mentioned TgCPL
333 is a major endopeptidase involved in the maturation of micronemal proteins and digestion of host proteins
334 [4,10]. Infected host cells were incubated with LHVS for 48 hrs to allow full inhibition of TgCPL. Treated
335 parasites were liberated from host cells and used to infect new host cells for 30 minutes, followed by TgCPL
336 staining to quantify the size of the VAC. As expected, LHVS-treated Δ*crt* parasites displayed smaller VACs
337 than DMSO-treated Δ*crt* parasites **(Fig 6A)**. TgCPB is another known VAC-localizing protease, displaying
338 both endo- and exo-peptidase activities [13,23]. Due to its carboxypeptidase activity, it is expected that
339 TgCPB generates more small solutes relative to TgCPL. We used CRISPR-Cas9 editing to generate a
340 Δ*crt*Δ*cpb* double knockout **(Fig 6B)**. The replacement of *TgCPB* with a pyrimethamine resistance cassette
341 was confirmed by PCR and immunoblotting **(Fig 6B)**. The resulting Δ*crt*Δ*cpb* mutant showed a smaller
342 concave subcellular structure compared to the Δ*crt* mutant **(Fig S3)**. The size of the VAC in WT, Δ*crt*, and
343 Δ*crt*Δ*cpb* was quantified based on the TgCPL staining as described above and the Δ*crt*Δ*cpb* parasite VAC
344 (0.85 ± 0.15 μm) was reduced by ~30% compared to Δ*crt* parasites (1.15 ± 0.10 μm) **(Fig 6C)**. The
345 moderate decrease in the size of the VAC in the Δ*crt*Δ*cpb* strain also reduced the number of parasites
346 showing partial overlap between the VAC and ELC. Approximately 44% of Δ*crt*Δ*cpb* parasites showed
347 partial overlap between TgCPL and proTgM2AP staining compared to 62% in the Δ*crt* strain (**Fig 6D**), with
348 both significantly higher than the 19% and 25% seen for WT and Δ*crtCRT* strains, respectively. TgSUB1
349 showed comparable expression in both the WT and Δ*crt*Δ*cpb* strains (**Fig 6E**). Similarly, TgSUB1 was
350 observed in both constitutive and induced ESA fractions in the Δ*crt*Δ*cpb* parasites (**Fig 6F**). TgM2AP and
351 TgMIC2 were cleaved by TgSUB1 in Δ*crt*Δ*cpb*, and their secretion patterns were similar to those seen in
352 the WT strain (**Fig 6F**). These partially restored phenotypes in the Δ*crt*Δ*cpb* mutant improved the invasion
353 efficiency by ~ 60% compared to the Δ*crt* strain, although invasion was still significantly lower than that of
354 WT parasites **(Fig 6G)**. Collectively, these data show a close association between the size of the VAC,

355 altered morphology of the parasite's endolysosomal system, protein abundance of TgSUB1, and parasite
356 invasion.
357
358 **8. TgCRT is a functional transporter.**
359 Finally, we attempted to express TgCRT in *S. cerevisiae* yeast following previously described
360 strategies for PfCRT [31,32]. Native *TgCRT* cDNA did not express well in *S. cerevisiae* yeast (**Fig S5**),
361 however, following a previously published strategy for difficult to express PfCRT mutants [20] we created
362 a fusion gene that replaced the 300 most N-terminal residues of the *TgCRT* sequence with 111 most N-
363 terminal residues from *S. cerevisiae* plasma membrane ATPase (PMA), which harbors a yeast plasma
364 membrane localization sequence (**Fig S4B and S4C**). Via alignment with PfCRT (**Fig S4A**), removing the
365 300 N-terminal TgCRT residues that are non-homologous to PfCRT preserves all putative
366 transmembraneous domains and inter helical loop regions. The fusion protein was well expressed in *S.*
367 *cerevisiae* (**Fig S5**). Following an approach previously described for PfCRT and PfCRT mutants [20,33]
368 we assayed PMA-TgCRT expressing yeast for chloroquine (CQ) transport **(Fig. 7A).** Via alignment with
369 PfCRT (**Fig S4A**), TgCRT T369 corresponds to the well-studied K76 residue within PfCRT; previously,
370 mutation of PfCRT K76 to T has been shown to increase the efficiency of CQ transport by PfCRT [20,34,35].
371 We individually expressed both WT TgCRT and a T369K variant in the yeast to measure their transport
372 efficiencies. Both the wild type protein and a TgCRT T369K mutant were found to transport CQ slower
373 than PfCRT under similar conditions and to require higher external [CQ] (80 mM versus 16 mM for PfCRT)
374 to achieve similar levels of transport (**Fig 7A**). These initial data have shown that mutation of the
375 corresponding TgCRT threonine to lysine affects CQ transport similarly.
376
377 We also exchanged threonine for lysine in the WT TgCRT complementation construct and transfected
378 Δ*crt* to examine the extent to which $TgCRT^{T369K}$ affects VAC size in *Toxoplasma* parasites. Interestingly,
379 in contrast to full recovery of VAC size in the WT TgCRT complementation strain, $TgCRT^{T369K}$ only partially
380 restored the swollen VAC (**Fig 7B**). These findings, along with the TgCRT transport data, strongly suggest

381 that the swollen VAC is caused by luminal osmolyte excess, similar to findings for PfCRT as described in
382 "Discussion".
383
384 In summary, our findings strongly suggest a role for TgCRT in small solute transport that regulates
385 VAC volume, similar to the role proposed for PfCRT [16,17]. However, at least for *T. gondii,* osmotic
386 pressure within this organelle regulated by the TgCRT protein governs proper segregation of other
387 organelles within the endolysosomal system that, in turn, facilitates microneme secretion and parasite
388 invasion. The data also indicate that the invasion deficiency exhibited by the Δ*crt* mutant is likely due to
389 multiple factors, since the recovery of TgSUB1 expression and micronemal trimming in Δ*crt*Δ*cpb* did not
390 completely reverse invasion defects. To our best knowledge, this is the first observation of regulation of
391 apicomplexan parasite invasion by a CRT protein.
392
393 **Discussion**
394 *Toxoplasma* utilizes an endolysosomal system to secrete invasion effectors that disseminate infection.
395 These invasion effectors undergo a series of intracellular proteolytic cleavage and trimming steps to reach
396 their final forms. Therefore, maintenance of the integrity of the endolysosomal system is critical for
397 controlling the secretion of invasion effectors in *Toxoplasma*. The Vacuolar Compartment (VAC) is an
398 acidic lysosome-like vacuole. Previous work showed that deletion of a cathepsin L-like protease, a major
399 VAC luminal endopeptidase, leads to invasion, replication, and virulence defects [4,10]. Compromised
400 proteolytic activities within these parasites also result in the inefficient degradation of endocytosed host
401 proteins [10]. Warring *et al.* previously reported that a *Toxoplasma* ortholog of chloroquine resistance
402 transporter (TgCRT) resides in the VAC and that decreased expression of TgCRT leads to swelling of the
403 VAC [14].
404
405 Here, we created a *TgCRT* knockout that completely removes *TgCRT* from the VAC membrane. The
406 resulting Δ*crt* strain shows a dramatic increase in VAC size, and the organelle aberrantly co-localizes with
407 the adjacent endosome-like compartment **(Fig 8)**. Although a previous study reported that parasites deliver

408 minor amounts of TgCPL to the ELC which then contributes to maturation of some micronemal proteins
409 [4], our data do not reveal abnormal intracellular cleavage or trafficking of micronemal proteins in Δ*crt*
410 parasites. Relatedly, Dogga *et al.* recently documented that aspartic acid protease 3 (TgASP3) localizes
411 in a post-Golgi compartment and serves as a major maturase for invasion effectors [5], suggesting that the
412 cleavage of micronemal proteins by TgCPL in the ELC plays only a minor role in their maturation.
413
414 We also measured the retention and secretion of micronemal proteins on the parasite's surface and in
415 the medium executed by TgROM4 and TgSUB1, respectively. We found that the micronemal proteins were
416 improperly trimmed on the surface of Δ*crt* parasites. Patterns of secreted micronemal proteins observed
417 for the Δ*crt* mutant were similar to those for Δ*sub1* parasites, which led us to examine the expression of
418 TgSUB1 in Δ*crt* parasites and ESAs. As expected, levels of TgSUB1 were decreased on the surface of
419 Δ*crt* parasites and in the medium during secretion. Interestingly, the steady state abundance of TgSUB1
420 was also significantly decreased in the Δ*crt* mutant. Surprisingly, we found that the reduction of TgSUB1
421 was due to a decrease in the transcription level of TgSUB1 in the Δ*crt* strain, suggesting that the parasites
422 utilize a feedback transcriptional mechanism to regulate TgSUB1.
423
424 TgSUB1 is a micronemal GPI anchored protein. It remains unclear how TgSUB1 becomes activated
425 within *Toxoplasma*. Previous pulse-chase experiments have revealed that TgSUB1 undergoes maturation
426 in a post-ER compartment, and passes through the endolysosomal system before its arrival at the
427 microneme and subsequent secretion [11]. The propeptide region of TgSUB1 carries targeting information
428 which helps to guide the protein to the microneme [36]. The propeptide may also function by binding to
429 active sites of mature TgSUB1 to inhibit its proteolytic activity during trafficking. Co-localization of the VAC
430 and ELC could bring propeptide-bound TgSUB1 to a protease-abundant environment, where non-specific
431 digestion of the propeptide could then lead to increased digestive activities in the VAC and ultimately result
432 in an increase in osmotic pressure within the hybrid VAC/ELC organelle **(Fig 8)**. During this scenario, the
433 parasites may utilize a feedback mechanism to repress additional expression of TgSUB1 in order to avoid
434 further VAC swelling. Moreover, we also discovered that the Δ*crt* parasites had reduced protein and/or

435 transcript levels of several other proteases, including two known VAC proteases, TgCPL and TgCPB.
436 Therefore, the parasites down-regulate a number of endolysosomal-VAC proteases to suppress proteolytic
437 activities in the swollen VAC, presumably to reduce osmotic pressure and thereby control VAC size.
438 Among these proteases, TgSUB1 has been shown to be involved in parasite invasion and virulence defects
439 but not replication and egress [3]. Additionally, TgCPL plays a role in parasite invasion by maturing several
440 micronemal proteins [4]. Therefore, the invasion defects exhibited in the Δ*crt* mutant could be due to
441 several factors.
442
443 Altered endolysosomal protease transcript levels in Δ*crt* parasites suggest that parasites repress
444 transcription factors or enhance transcription repressors to respond to increased VAC size. RNA-Seq
445 analysis did not reveal any changes in the AP2-family of transcription factors (data not shown). In
446 mammalian cells, the transcription factor EB (TFEB) is a master regulator that drives gene expression for
447 autophagy and lysosome biogenesis [37]. Search of the *Toxoplasma* genome did not reveal a TgTFEB
448 ortholog, suggesting that these parasites may adopt an alternative strategy for regulating lysosomal gene
449 expression. Interestingly, our differential gene expression analysis identified that the transcript levels of
450 two zinc finger (CCCH) type motif-containing proteins, TGGT1_246200 and TGGT1_226310, were
451 increased and decreased by 2-fold and 3-fold (**Table S1**), respectively, in the Δ*crt* mutant. The CCCH type
452 zinc finger motif-containing protein is known to regulate the stability of mRNA [38]. For example,
453 tristetraprolin inhibits the production of tumor necrosis factor-α in macrophages by destabilizing its mRNA
454 via an interaction with AU-rich elements at the 3'-untranslated region [39]. Further investigation to identify
455 transcription factor(s) and regulator(s) that govern the expression of *Toxoplasma* lysosomal genes will help
456 elucidate how these parasites regulate the biogenesis and function of the VAC.
457
458 In this study, we have determined that *TgCRT*-deficient parasites have reduced expression of several
459 endolysosomal proteases. We have also found that suppression of proteolytic activities within the swollen
460 VAC decreases the size of the organelle. These findings, along with data verifying that TgCRT is indeed a
461 transporter with function similar to that of PfCRT, support the idea that TgCRT functions to transport

462 essential VAC osmolytes, similar to proposals for PfCRT [16,17,40]. Likely candidate osmolytes include
463 ions and/or amino acids. We suggest that when TgCRT is absent on the membrane of the VAC, protein
464 degradation products (short peptides, amino acids) likely accumulate within the VAC and increase osmotic
465 pressure, thereby leading to the swollen phenotype. Consistent with this idea, and similar to related
466 observations for *P. falciparum* treated with cysteine protease inhibitors [41], chemical inhibition of
467 proteolysis via the small inhibitor LHVS dramatically reduces the size of the VAC. For *Toxoplasma*, LHVS
468 principally targets TgCPL, but also binds to TgCPB protease [13]. Additionally, the maturation of TgCPB
469 is dependent upon the presence of TgCPL [13]. Therefore, the treatment of LHVS blocks both of these
470 VAC proteases. Since the cathepsin B (TgCPB) protease exhibits endo- and exo-peptidase activities, and
471 the deletion of TgCPB had no effect on the abundance of TgCPL [13], we genetically ablated *TgCPB* to
472 further understand its role in regulating VAC morphology. The deletion of *TgCPB* partially restored the size
473 of the VAC, secretion patterns of micronemal proteins, and invasion defects. These results reveal for the
474 first time that TgCPB plays an active role in contributing to proteolysis within the VAC in *Toxoplasma*
475 parasites.
476
477 RNA-Seq analysis identified several other genes with altered transcription levels, suggesting that the
478 parasites may utilize additional strategies to control VAC size. For example, interestingly, levels of
479 aquaporin (TGGT1_215450) transcript were reduced in Δ*crt* parasites. Previous work showed that this
480 aquaporin is localized to the VAC/PLV [42]. Therefore, it seems likely that Δ*crt* parasites express less
481 aquaporin to reduce water transport into the VAC/PLV, as an additional tactic to limit VAC swelling. We
482 also found that two putative protein phosphatase 2C (TGGT1_276920 and TGGT1_201520) transcripts
483 are down-regulated in the Δ*crt* mutant. Both carry signal peptides, indicating endosomal trafficking.
484 TGGT1_276920 and TGGT1_201520 are homologous to PTC3 and PTC1 in *S. cerevisiae,* respectively.
485 Interestingly, both PTC1 and PTC3 proteins are involved in yeast osmosensory regulation. A mitogen-
486 activated protein kinase pathway is activated when yeast cells experience hyperosmotic conditions. PTC1
487 and PTC3 negatively regulate this pathway [43,44]. Furthermore, PTC1 was found to control the function
488 and morphology of the yeast vacuole, which further alters its biogenesis [45]. The dramatic change in

489 *Toxoplasma* VAC volume indicates induced osmotic stress in the Δ*crt* parasites. The knockout parasites
490 appear to be utilizing a similar mechanism to suppress these protein phosphatases and enhance similar
491 osmoregulatory signaling. We suggest similar studies for *P. falciparum* and other apicomplexan parasites
492 that express CRT orthologs would be informative.
493
494 The phenotype of the swollen VAC in the Δ*crt* strain mirrors the enlarged digestive vacuole in
495 chloroquine (CQ) resistant (CQR) *P. falciparum* malaria [16]. Peptidomic analysis showed that hemoglobin
496 is not as efficiently degraded within the digestive vacuole (DV) in CQR malaria parasites [40], further
497 suggesting that CQR mutations in PfCRT alter the physiology within the swollen digestive vacuole, thereby
498 compromising DV proteolytic activities. *In vitro* assays utilizing recombinant PfCRT, reconstituted in
499 proteoliposomes, have revealed that PfCRT may act as a proton gradient dependent, polyspecific nutrient
500 exporter for small solutes including amino acids, oligopeptides, glutathione, and small drugs [18,19]. These
501 studies also demonstrate that CQR-associated PfCRTs display altered transport efficiency relative to CQ-
502 associated PfCRT. Our study has revealed that TgCRT mediates CQ transport similar to PfCRT. The Δ*crt*
503 strain appears more sensitive to CQ relative to WT parasites (**Fig S6**), further suggesting that TgCRT is a
504 functional transporter of small solutes across the membrane of the VAC. We suggest that alteration of
505 proteolytic activities in the enlarged VAC of the Δ*crt* mutant reveals a similar scenario relative to the CQR
506 *P. falciparum* DV. Given the similarity in components and functionality of the VAC and DV found in
507 *Toxoplasma* and *Plasmodium*, this *Toxoplasma TgCRT*-deficient mutant should prove useful for further
508 studying the native function of CRT orthologs from other apicomplexan parasites.
509
510 In sum, our findings reveal that the *Toxoplasma* TgCRT protein is indeed a small molecule transporter
511 that plays an essential role in regulating the size and morphology of the VAC. Unexpectedly, this regulation
512 maintains integrity of the parasite's endolysosomal system, which is essential for the trafficking of invasion
513 effectors. Co-localization of the VAC and endosome-like compartment in the *TgCRT* knockout led to a
514 reduction in transcript and protein levels for several endolysosomal proteases. We found that blocking
515 normal proteolysis within the swollen VAC reduced the size and partially restored the morphology of the

516 organelle. Taken together, these findings suggest that TgCRT mediates the transport of small solutes in
517 order to regulate VAC size and morphology. The data show that the integrity of the parasite endolysosomal
518 system is critical for parasite virulence. We suggest that pharmaceutical modulation of the VAC could serve
519 as a novel strategy for managing toxoplasmosis.
520

521 **Materials and Methods**

522 **Ethical statement**

523 This study was performed in compliance with the Public Health Service Policy on Humane Care and
524 Use of Laboratory Animals and Association for the Assessment and Accreditation of Laboratory Animal
525 Care guidelines. The animal protocol was approved by Clemson University's Institutional Animal Care and
526 Use Committee (Animal Welfare Assurance A3737-01, protocol number AUP2016-012). All efforts were
527 made to minimize discomfort. This method of euthanasia is consistent with the recommendations of the
528 Panel on Euthanasia of the American Veterinary Medical Association.

529

530 **Chemicals and reagents**

531 Morpholine urea-leucyl-homophenyl-vinyl sulfone phenyl (LHVS) was kindly provided by the Bogyo
532 lab at Stanford University. Other chemicals used in this work were analytical grade and were purchased
533 from VWR unless otherwise indicated.

534 **Parasite culture**

535 *Toxoplasma gondii* parasites were cultured in human foreskin fibroblast (HFF) cells (ATCC, SCRC-
536 1041) in Dulbecco's Modified Eagle Medium (DMEM) media supplemented with 10% cosmic calf serum at
537 37 °C with 5% CO_2. The parasites were harvested by membrane filtration as described previously [13].

538

539 **Generation of transgenic parasites**

540 To generate the TgCRT-deficient strain, ~1.5 kilobases (kb) of the 5'- and 3'-UTR of the *TgCRT* gene,
541 respectively, were PCR-amplified and flanked at both ends of the bleomycin resistance cassette (BLE) to
542 assemble a *TgCRT* deletion construct. The resulting plasmids were introduced into WT parasites by
543 electroporation. The transfected parasites were selected with 50 µg/ml bleomycin twice, while in their
544 extracellular stage as described previously [13]. Clones of the TgCRT-deficient parasites were isolated by
545 limiting dilution. The correct replacement of *TgCRT* with the *BLE* cassette was confirmed by quantitative
546 PCR (see text).

547

548 To complement Δ*crt* parasites, we modified the plasmid pTub-TgCRT-mCherry-3xmyc (a gift from the
549 van Dooren lab), which expresses a C-terminally mCherry-3xmyc epitope-tagged TgCRT under the
550 *Toxoplasma* tubulin promoter. The plasmid was restricted with HpaI and MfeI to remove the tubulin
551 promoter and a segment of *TgCRT*. The remaining DNA fragment served as the backbone for subsequent
552 Gibson assembly to incorporate a PCR amplified ~1 kb region upstream of the *Tgku80* gene, the ~1 kb
553 fragment of the *Tgcrt* 5'-UTR region, and the removed partial *Tgcrt* coding sequence to produce the TgCRT
554 complementation plasmid, pCRT-TgCRT-mCherry-3xmyc. The complemented TgCRT is driven by its
555 cognate promoter to maintain physiologic similarity to native TgCRT expression in WT parasites (see text).
556 The 1 kb region located ~6 kb upstream of the *Tgku80* gene was used to facilitate a single integration of
557 the TgCRT complementation plasmid into this specific locus by single crossover homologous
558 recombination. The TgCRT complementation construct was digested with SwaI restriction enzyme, gel-
559 extracted, purified, and transfected into Δ*crt* parasites by electroporation.
560
561 To introduce NanoLuc® luciferase (nLuc) into parasites, we PCR-amplified and assembled the
562 *Tgtubulin* promoter, the coding sequence of the nLuc luciferase, and an HXG selection marker into an
563 nLuc expression construct. The resulting plasmid was transfected into WT, Δ*crt*, and Δ*crtCRT* strains. The
564 transfectants were selected with 25 µg/ml mycophenolic acid and 50 µg/ml xanthine. Stable populations
565 were subjected to limiting dilution to generate individual clones of WT::*nLuc*, Δ*crt*::*nLuc*, and Δ*crtCRT*::*nLuc*
566 and clones were confirmed via luciferase activity.
567
568 To generate the Δ*crt*Δ*cpb* mutant, the *TgCPB* gene was replaced with a pyrimethamine resistance
569 cassette using the CRISPR-Cas9 genome editing system [46,47]. The pyrimethamine resistance cassette
570 was PCR-amplified and flanked by 50 bp regions upstream and downstream of the start and stop codons
571 of the *TgCPB* gene for homologous recombination. A 20 bp region located at the beginning of the coding
572 region of the *TgCPB* gene was used to design guide RNA and replace the guide RNA targeting TgUPRT
573 gene in the plasmid pSAG1-Cas9::UPRTsgRNA using Q5 site-directed mutagenesis (NEB). The Cas9-
574 GFP and guide RNA constructs were co-transfected into Δ*crt* parasites with the corresponding repair PCR

575 product. The guide RNA and Cas9 generated a gap within the *TgCPB* gene to facilitate double crossover
576 homologous recombination. Correct gene replacement was confirmed by PCR.
577
578 To epitope-tag TgAMN, we again used CRISPR-Cas9 editing tools to modify the corresponding gene.
579 Guide RNA recognizing the 20 bp region near the TgAMN stop codon was generated using the methods
580 above.
581
582 The 50-bp homologous regions upstream and downstream of the stop codon of the *TgAMN* gene were
583 cloned at the 5'- and 3'-ends of the DNA sequence containing the 3xHA epitope tag and the pyrimethamine
584 resistance cassette, respectively, by PCR. The plasmid encoding the guide RNA targeting TgAMN and
585 Cas9-GFP and the PCR product were co-transfected into WT parasites. The stop codon of TgAMN was
586 replaced by the 3xHA epitope tag and pyrimethamine resistance cassette. Stable populations were
587 generated after multiple rounds of pyrimethamine selection and TgAMN-3xHA fusion protein was
588 confirmed by immunoblotting analysis.
589
590 TgSCP was endogenously tagged with a 3xmyc epitope tag via single crossover. An approximately 1
591 kb region upstream of the *TgSCP* stop codon was PCR amplified and fused in frame with a 3xmyc epitope
592 to assemble TgSCP-3xmyc. A pyrimethamine resistance cassette was also included, the resulting plasmid
593 was linearized and transfected into WT parasites. The correct tagging was confirmed by immunoblotting.
594
595 **Site-directed mutagenesis**
596 Threonine 369 was mutated to lysine in the WT TgCRT complementation construct, via site directed
597 mutagenesis according to the Q5® site-directed mutagenesis procedure (NEB). Linear PCR product was
598 phosphorylated, circularized, and transformed into *E. coli*. Correct clones were identified by direct DNA
599 sequencing.
600
601 **Transfection of *Toxoplasma* parasites**

602 *T. gondii* parasites were allowed to grow in HFF cells for 48 hrs at 37 °C with 5% CO_2. Freshly egressed
603 parasites were syringed, filter purified, and harvested in Cytomix buffer (25 mM HEPES, pH 7.6, 120 mM
604 KCl, 10 mM K_2HPO4/ KH_2PO4, 5 mM $MgCl_2$. 0.15 mM $CaCl_2$, and 2 mM EGTA). Parasites were pelleted
605 at 1,000x *g* for 10 min, washed once in Cytomix buffer, and resuspended in Cytomix buffer at 2.5 x 10^7
606 parasites per ml. 400 µL of parasite suspension was mixed with 20 µg DNA and 2 mM ATP/5 mM reduced
607 glutathione to a final volume of 500 µL. The mixture was electroporated at 2 kV and 50 ohm resistance
608 using the BTX Gemini X2 (Harvard Apparatus). Transfectants were inoculated into a T25 flask pre-seeded
609 with confluent monolayer of HFF cells and the cells allowed to recover. Drug selection was applied 24 hrs
610 post transfection.
611
612 **Immunofluorescence**
613 Freshly lysed parasites were used to infect confluent HFF cells pre-seeded in an 8-well chamber slide
614 for 1 hr (pulse invaded parasites) or 18-24 hrs (replicated parasites). The extracellular parasites were
615 attached to chamber slides using 0.1% (w/v) poly-L-lysine. Immunofluorescence was performed as
616 described previously [10,13]. Images were viewed and digitally captured using a Leica® CCD camera
617 equipped with a DMi8 inverted epifluorescence microscope and processed with Leica® LAS X software.
618
619 **Excretory secretory antigens (ESAs) preparation**
620 Freshly egressed parasites were syringed, filter purified, and resuspended at 5 x 10^8 parasites/ml in
621 D1 medium (DMEM medium supplemented with 1% FBS). 100 µL of parasite suspension was transferred
622 to a microfuge tube and incubated at 37 °C for 30 min to prepare constitutive ESAs. To isolate induced
623 ESAs, the parasite suspension was incubated in D1 medium supplemented with 1% ethanol for 2 min at
624 37ºC. ESAs were separated from intact parasites by centrifugation at 1,000 x *g* for 10 min. ESA fractions
625 were transferred to a new microfuge tube, mixed with SDS-PAGE sample loading buffer, and boiled for 5
626 min for immunoblotting analysis.
627
628 **SDS-PAGE and Immunoblotting**

629 Parasite lysates and ESA fractions were prepared in 1x SDS-PAGE sample buffer and boiled for 5 min
630 before resolving on standard SDS-PAGE gels. For immunoblotting, gels were transferred to PVDF
631 membranes by semi-dry protein transfer methods. Blots were blocked with 5% non-fat milk and incubated
632 with primary antibody diluted in 1% non-fat milk. Goat anti-mouse or anti-rabbit IgG antibodies conjugated
633 with horseradish peroxidase were used as secondary antibody. Immunoblots were developed with
634 SuperSignal™ WestPico chemiluminescent substrate (Thermo). The chemiluminescence signals were
635 captured using the Azure® Imaging System. Bands were quantified by densitometry using LI-COR® Image
636 Studio software.
637
638 **Parasite invasion assay**
639 The red-green invasion assay was used to measure the efficiency of parasite invasion. Freshly purified
640 parasites were syringed, filter purified, and resuspended at 5 x 10^7 parasites/ml in invasion medium (DMEM
641 supplemented with 3% FBS). 200 µL of parasite resuspension was inoculated into each well of an 8-well
642 chamber slide pre-seeded with HFF cells, and parasites were allowed to invade host cells for 30, 60, and
643 120 min before fixation with 4% formaldehyde for 20 min. Before membrane permeabilization, slides were
644 stained with mouse anti-TgSAG1 monoclonal antibody (1:1,000) for 1 hr to label attached parasites. After
645 treatment with 0.1% Triton X-100 for 10 min, the parasites were stained with rabbit polyclonal anti-TgMIC5
646 antibody (1:1,000) for 1 hr to stain both invaded and attached parasites. Subsequently, slides were stained
647 with goat anti-mouse IgG conjugated with Alexa 594 (red) (Invitrogen, 1:1,000) and goat anti-rabbit IgG
648 conjugated with Alexa 588 (green) (Invitrogen, 1:1,000) along with DAPI for nuclear staining. After staining,
649 slides were mounted with anti-fade Mowiol solution and observed by immunofluorescence. Extracellular
650 parasites only showed red fluorescence, whereas intracellular parasites exhibited both red and green
651 fluorescence. Six fields of view from individual invasion experiments were captured by a Leica® DMi8
652 inverted epifluorescence microscope and processed with ImageJ software. The attachment efficiency of
653 each strain was measured by dividing the total number of parasites labeled in red by the total number of
654 host nuclei, and normalized against that of WT parasites. The invasion efficiency of each strain was

655 quantified using the following equation ([sum of green parasites] − [sum red parasites])／total host nuclei,
656 and data were normalized against data for WT parasites.
657
658 **Immunofluorescence-based replication assay**
659 Freshly egressed parasites were filter-purified and inoculated into individual wells of an 8-well chamber
660 slide pre-seeded with HFF cells at approximately 1 x 10^5 cells per well. Non-invaded parasites were
661 washed off at 4 hrs post-infection. Invaded parasites were allowed to infect host cells for an additional 24
662 and 32 hrs before fixation. The infected host cells were stained with monoclonal anti-TgGRA7 (1:1,000)
663 antibody and DAPI to help distinguish individual parasitophorous vacuoles (PVs) and the nuclei of
664 parasites, respectively. Slides were subjected to standard immunofluorescence microscopy for imaging.
665 100 parasitophorous vacuoles were enumerated for each strain and plotted as the distribution of different
666 sized PVs. In addition, replication was also expressed as the average number of parasites per PV.
667
668 **Luminescence-based growth assay**
669 Parasites expressing NanoLuc luciferase were inoculated into a white 96-well tissue culture plate with
670 a flat, solid bottom (Greiner Bio-One) pre-seeded with confluent HFF cells at 1.5 x 10^3 cells/well. Each
671 strain was inoculated into 4 individual wells to monitor the fold-change of luciferase activity versus time,
672 which is proportional to intracellular growth. At 4 hrs post-infection, the individual wells were aspirated to
673 remove non-invaded parasites. The first well was treated with 100 µL of lysis buffer containing NanoLuc
674 luciferase substrate and incubated for 10 min, and a luminescence reading was taken by using the BioTek®
675 multimode H1 hybrid plate reader. The remainder of the 3 wells were replenished with fresh D10 medium
676 without phenol red for an additional 24, 48, and 72 hrs. Subsequent luminescence readings were all
677 performed via the methods above. Luminescence readings versus time were normalized against the
678 reading at 4 hrs post-infection to calculate the fold-change of parasite growth.
679
680 **Egress assay**

681 A Lactate dehydrogenase release assay was used to measure the egress efficiency of parasites.
682 Freshly lysed parasites were filter-purified and resuspended in D10 medium at 5 x 10^5 parasites/ml. 100
683 µL of parasite suspension was inoculated into each well of a 96-well plate pre-seeded with HFF cells. The
684 parasites were allowed to replicate for 18-24 hrs, washed, and incubated with 50 µl of Ringer's buffer (10
685 mM HEPES, pH 7.2, 3 mM HaH_2PO_4, 1 mM $MgCl_2$, 2 mM $CaCl_2$, 3 mM KCl, 115 mM NaCl, 10 mM glucose,
686 and 1% FBS) for 20 min. Subsequently, an equal volume of 1 mM Zaprinast dissolved in Ringer's buffer
687 was added to the wells and incubated for 5 min at 37ºC and 5% CO_2. Uninfected wells were treated with
688 50 µl of Ringer's buffer containing 1% Triton X-100 or normal Ringer's buffer, serving as positive and
689 negative controls, respectively. The released lactate dehydrogenase was centrifuged at 1,000 *x g* for 5
690 min twice to pellet insoluble cell debris. Fifty microliters of supernatant was subjected to the standard
691 lactate dehydrogenase release assay as described previously [48]. The egress efficiency of each strain
692 was calculated using the following equation, ([LDH activity derived from individual parasites]− [LDH activity
693 of negative control])／([LDH activity of positive control]−[LDH activity of negative control]), and normalized
694 against data for WT parasites.
695
696 **Size measurement of the VAC**
697 The size of the VAC was quantified based on TgCPL staining (TgCPL is a VAC luminal protease).
698 Freshly purified parasites were inoculated into pre-seeded HFF chamber slides, allowed to invade host
699 cells for 30 min prior to fixation, stained with polyclonal rabbit anti-TgCPL antibody (1:100), and VAC
700 diameter measured by immunofluorescence microscopy. The distance of the widest diagonal of TgCPL
701 staining was used as the diameter of the VAC and was quantified using Leica® LAS X software.
702 Measurements for 50 individual parasites were performed for each replicate, data are presented as
703 average ± S.D..
704
705 **Transcriptome sequencing and quantitative PCR (qPCR) assay**
706 Total RNA was extracted from freshly lysed parasites using the Zymo® Direct-zol™ RNA MiniPrep Plus
707 kit, and converted to sequencing read libraries using the TruSeq Stranded mRNA sequencing kit (Illumina).

708 The prepared libraries were subjected to 2 x 125 bp paired-end Illumina® HiSeq2500 sequencing. Each
709 sample was sequenced to a depth of at least 20 million reads. Differential expression profiling was
710 performed by the Clemson University Genomics Computational Lab.
711
712 Approximately 500 ng of total RNA was used to measure the steady levels of transcripts for individual
713 genes by using the Luna® Universal One-Step RT-PCR kit (NEB). The qPCR assay was performed using
714 the BioRad CFX96 Touch™ Real-Time PCR detection system. The quantification cycle (Cq) values for
715 individual genes were used for double delta Cq analysis to calculate their relative abundances to that of
716 WT parasites using the Bio-Rad® CFX Maestro™ software. TgActin was used as the housekeeping gene
717 for normalization.
718
719 **Mouse studies**
720 Six- to eight-week-old, outbred CD-1 mice were infected by subcutaneous or intravenous injection with
721 100 WT or mutant parasites diluted in PBS. The infected mice were monitored for symptoms daily for a
722 total of 30 days. Mice that appeared moribund were humanely euthanized via CO_2 overdose, in compliance
723 with IACUC's approved protocol. The seroconversion of the surviving mice was tested by enzyme-linked
724 immunosorbent assay (ELISA). The surviving mice were allowed to rest for 10 days, prior to subcutaneous
725 injection with a challenge dose of 1000 WT parasites, and were monitored daily for survival for 30 days.
726
727 **Generation of TgCRT expression construct in yeast**
728 *TgCRT* cDNA was PCR amplified from pTub-TgCRT-mCherry-3xmyc plasmid using a forward primer
729 that introduced a 5' KpnI site and *S. cerevisiae* Kozak sequence, and a reverse primer that omitted the
730 mCherry-3xmyc tag and introduced a 3' XmaJI site. The PCR amplified DNA was digested with KpnI and
731 XmaJI and subcloned into pYES2-6xHis-BAD-V5 (hexa His, biotin acceptor domain, V5 tags) plasmid
732 behind the GAL1 promoter and in front of the His-BAD-V5 epitope tags to generate the plasmid
733 pYES/TgCRT-hbv. To generate the plasmid pYES/PMA-TgCRT-hbv, DNA encoding TgCRT-hbv was PCR
734 amplified using a forward primer that omitted the first 900 bases of TgCRT and introduced a 5' SacI site,

735 and a reverse primer that included a 3' NotI site and His-BAD-V5 tags. The amplified DNA was digested
736 with SacI and NotI and subcloned into a SacI/NotI-digested pYES/PfHB3$_{PMA}$ (from [32]; modified via site-
737 directed mutagenesis to introduce a SacI site at the PMA-PfCRT interface). Mutagenesis reactions were
738 performed using reagents obtained from Agilent (Santa Clara, CA).
739
740 **Preparation of Yeast Membrane and Western blotting**
741 Isolation of yeast membranes and detection of proteins by Western blot were as described in [20].
742
743 **Measurement of CQ incorporation in yeast expressing CRT**
744 Quantitative growth rate analysis was used to calculate CQ transport as previously described in detail
745 elsewhere [20,32,33]. Briefly, growth under each condition was measured in duplicate at an initial cell
746 density of OD_{600}=0.1 in 96-well plates placed in a Tecan (Durham, NC) M200Pro or BioTek (Winooski, VT)
747 Epoch2 plate reader. CQ-induced growth delays at 80 mM CQ, pH 6.75 were calculated as the difference
748 in time taken to reach maximal growth rate in PMA-TgCRT non-inducing versus inducing media (see [33]).
749
750 **Statistics**
751 Statistical analysis was performed using Prism software (GraphPad). The methods used in different
752 assays were indicated in the figure legends.

Table 1. Strains used in this study

Name	Genetic background	Comments
WT	RH*Δku80Δhxg*	Requested from the Carruthers Lab, not generated in this study
Δcrt	RH*Δku80Δhxg Δcrt*	*TgCRT* was deleted by double crossover homologous recombination
ΔcrtCRT	RH*Δku80Δhxg Δcrt*::*TgCRT-mCherry-3xmyc*	Ectopic expression of a C-termially epitope-tagged TgCRT in *Δcrt* for complementation
ΔcrtCRT^{T369K}	RH*Δku80Δhxg Δcrt*::*TgCRT*^{T369K}*-mCherry-3xmyc*	Ectopic expression of a C-termially epitope-tagged TgCRT mutant in *Δcrt* for complementation. The original threonine at position 369 within TgCRT was changed to lysine by site-directed mutagenesis.
Δcrt Δcpb	RHΔku80Δhxg*Δcrt Δcpb*	The entire *TgCPB* gene was ablated by CRISPR-Cas9 based genome editing technique
WT::*nLuc*	RH*Δku80Δhxg*::*nLuc*	Expressed NanoLuc luciferase in WT parasites
Δcrt::*nLuc*	RH*Δku80Δhxg Δcrt*::*nLuc*	Expressed NanoLuc luciferase in *Δcrt* parasites
ΔcrtCRT::nLuc	RH*Δku80Δhxg Δcrt*::*TgCRT-mCherry-3xmyc::nLuc*	Expressed NanoLuc luciferase in *ΔcrtCRT* parasites
TgAMN-3xHA	RH*Δku80ΔhxgTgAMN-3xHA*	*TgAMN* gene was endogenously tagged with a 3xHA epitope at its 3'-end by CRISPR-Cas9 based genome editing technique
TgSCP-3xmyc	RH*Δku80ΔhxgTgSCP-3xmyc*	*TgSCP* gene was endogenously tagged with a 3xmyc epitope at its 3'-end by single crossover recombination

754 **Data Availability Statement:** The raw data of transcriptomic sequencing of WT and Δ*crt* strains have
755 been deposited in the NIH Gene Expression Omnibus (GEO) database. The accession number is
756 GSE116539. https://www.ncbi.nlm.nih.gov/geo/query/acc.cgi?acc=GSE116539
757
758 **Funding:** This work was supported by Knights Templar Eye Foundation Pediatric Ophthalmology Career-
759 Starter Research Grant (to Z.D.), a pilot grant of an NIH COBRE grant P20GM109094 (to Z.D.), the
760 Clemson Startup fund (to Z.D.), and NIHR01AI111962 and R01AI056312 (to P.D.R). The funders had no
761 role in study design, data collection and analysis, decision to publish, or preparation of the manuscript.
762
763 **Competing Interests:** The authors have declared that no competing interests exist.
764
765 **Acknowledgments**
766 We thank our colleagues Drs. Michael Blackman, Peter Bradley, Vern Carruthers, Silvia Moreno, and
767 David Sibley for kindly providing key reagents for this study. We also want to thank Drs. Rooksana Noorai
768 and Vijay Shankar at Clemson University Genomics Computational Lab for providing technical assistance
769 and expertise in performing transcriptomic sequencing and differential gene expression analysis and
770 depositing the raw data files of transcriptomic sequencing into the NIH GEO database. We acknowledge
771 Dr. Lesly Temesvari for critically reading this manuscript before submission.
772
773 **Author Contributions**
774 **Conceptualization:** Paul D. Roepe, Zhicheng Dou.
775 **Formal analysis:** L. Brock Thornton, Paige Teehan, Katherine Floyd, Christian Cochrane, Amy Bergmann,
776 Bryce Riegel, Paul D. Roepe, Zhicheng Dou.
777 **Funding acquisition:** Paul D. Roepe, Zhicheng Dou.
778 **Investigation:** L. Brock Thornton, Paige Teehan, Katherine Floyd, Christian Cochrane, Amy Bergmann,
779 Bryce Riegel, Zhicheng Dou.
780 **Methodology:** L. Brock Thornton, Paige Teehan, Bryce Riegel, Paul D. Roepe, Zhicheng Dou.

Project administration: Paul D. Roepe, Zhicheng Dou.

Resources: Paige Teehan, Amy Bergmann, Bryce Riegel, Zhicheng Dou.

Supervision: Paul D. Roepe, Zhicheng Dou.

Writing – original draft: Zhicheng Dou.

Writing – review & editing: L. Brock Thornton, Bryce Riegel, Paul D. Roepe, Zhicheng Dou.

787 **Figure legends:**

788 **Figure 1. The TgCRT-deficient parasites displayed a swollen digestive vacuole and a disrupted**
789 **endolysosomal system. A)** Schematic illustration of the strategies for the *Tgcrt* deletion and
790 complementation in *Toxoplasma* parasites. The plasmid carrying a bleomycin resistance cassette (*BLE*)
791 flanked by the *TgCRT* targeting sequences was transfected into WT parasites for double crossover
792 replacement of *TgCRT* to produce the Δ*crt* strain. The TgCRT complementation plasmid, containing the
793 coding sequence of TgCRT fused with mCherry and 3xmyc epitope tags at its C-terminus, was introduced
794 into the Δ*crt* strain to produce the Δ*crtCRT* complementation strain. **B)** The primers indicated in panel A
795 were used to verify the correct replacement of *TgCRT* with *BLE* by PCR. **C)** The complemented *TgCRT*
796 gene was transfected into Δ*crt* parasites and was verified by PCR. Since we complemented Δ*crt* with the
797 coding sequence of *TgCRT*, the PCR product was a 0.2 kb fragment in the Δ*crtCRT* strain, whereas
798 showing a 1.5 kb product in the WT strain whose *TgCRT* gene contains the introns. **D)** Transcript levels of
799 *TgCRT* in the WT, Δ*crt*, and Δ*crtCRT* strains were evaluated by quantitative PCR. Primers were designed
800 to anneal to the exons of *TgCRT* and are indicated in panel A. The *Tgactin* gene was included as a control
801 for normalization. The quantification of transcripts was performed in at least three biological replicates and
802 analyzed using unpaired Student's *t*-test. **E)** Extracellular Δ*crt* parasites showed an enlarged concave
803 subcellular structure, indicated by the arrow, under the differential interference contrast (DIC) microscopy.
804 Scale bar = 5 μm. **F)** The swollen subcellular structure indicated by the arrowhead was also observed in
805 pulse invaded Δ*crt* parasites and co-localized with a major luminal peptidase of the VAC, cathepsin L-like
806 protease (TgCPL). The TgCPL staining was used to assess the morphology of the VAC. The parasites
807 were allowed to invade host cells for 30 min before TgCPL antibody staining. The distance of the widest
808 diagonal of the TgCPL staining was determined to be the diameter of the VAC and was measured using
809 the Leica® LAS X software. The measurements were conducted in three biological replicates.
810 Measurements from 50 individual parasites from one representative assay were shown. The mean VAC
811 size ± SD was calculated for three independent measurements and is listed on the figure. Statistical
812 significance was determined using unpaired Student's *t*-test. Scale bar = 2 μm. **G)** Parasites were co-
813 stained with anti-TgCPL (the marker of the VAC) and anti-proM2AP or anti-TgVP1 (both are the markers

814 of the endosome-like compartment, ELC). In pulse invaded parasites, the VAC and ELC staining were
815 juxtaposed in the WT and Δ*crtCRT* strains, but aberrantly co-localized in the Δ*crt* strain. During replication,
816 the VAC in WT and Δ*crtCRT* parasites became fragmented. However, the abnormal co-localization of the
817 VAC and ELC significantly decreased the extent of VAC fragmentation in the Δ*crt* mutant. A major TgCPL
818 punctum existed in the replicated Δ*crt* parasites, not in WT and Δ*crtCRT* strains, and co-localized with
819 proTgM2AP and TgVP1 (indicated by arrows in the insets). The scale bars in the images of pulse invaded
820 and replicated parasites are 2 μm and 5 μm, respectively. ****, $p<0.0001$; n.s., not significant.
821
822 **Figure 2. Parasite invasion and acute virulence were reduced in the Δ*crt* parasites. A)** WT, Δ*crt*, and
823 Δ*crtCRT* parasites were allowed to invade host cells for 30, 60, and 120 min prior to fixation and antibody
824 staining. Parasites and host cells within six fields of view were counted for each strain. At least three
825 independent invasion assays were conducted for statistical analysis. The Δ*crt* parasites showed a ~50%
826 reduction in invasion at 30 min post-infection. The extent of the invasion defect in the Δ*crt* mutant was
827 gradually minimized overtime. At 60 min post-infection, there was approximately a 25% reduction in
828 invasion in Δ*crt* mutant, while there were no significant differences among the three strains at 120 min
829 post-infection. The assay was performed at least in triplicate. Statistical significance was determined using
830 unpaired Student's *t*-test. **B)** We infected confluent HFFs with WT, Δ*crt*, and Δ*crtCRT* parasites for 28 and
831 40 hrs before fixation and staining. Infected cells were stained with DAPI and anti-TgGRA7 antibodies in
832 order to recognize individual parasites and parasitophorous vacuoles, respectively. One hundred
833 parasitophorous vacuoles (PVs) were enumerated for the number of parasites they contained and the
834 distribution of different sized PVs was plotted. The average number of parasites per PV was also calculated
835 and listed above the plots. In addition, the growth rates of these strains were determined at 24, 48, and 72
836 hours by using a luminescence-based assay. Parasites were inoculated into a 96-well plate pre-seeded
837 with HFFs prior to lysis and quantification of luminescence activities at pre-determined time intervals. At
838 least three biological replicates were performed for the replication assay. Unpaired Student's *t*-test was
839 performed to calculate the statistical significance of parasite growth between strains. **C)** To measure the
840 egress of the parasites, 5×10^4 parasites were used to infect confluent HFFs in a 96-well plate for 24 hrs.

841 Replicated parasites were treated with 500 μM Zaprinast for 5 min at 37ºC and 5% CO_2 to induce egress.
842 Disruption of host cell membranes due to parasite egress released lactate dehydrogenase into the
843 medium, which was quantified and plotted. Unpaired Student's *t*-test was used to calculate the statistical
844 significance. There were no differences observed in parasite egress between WT and Δ*crt* parasites. **D)**
845 The acute virulence of TgCRT-deficient parasites was evaluated in a murine model via subcutaneous and
846 intravenous infections. One hundred parasites from each strain were used to infect outbred CD-1 mice
847 (n=10 mice for each strain). The mortality of the mice was monitored for 30 days. Seroconversion of the
848 surviving mice was evaluated by ELISA to confirm successful infection. Additionally, the surviving mice
849 were allowed to rest for 10 days before subsequent challenge with 1,000 WT parasites by subcutaneous
850 inoculation. The Δ*crt* mutant exhibited reduced acute virulence compared to the WT and Δ*crtCRT* strains
851 and conferred immunological protection in the surviving mice. Data were recorded and are presented using
852 the Kaplan-Meier plot. Statistical analysis was performed using the Log-rank (Mantel-Cox) test. For all
853 statistical significance calculation, *, $p<0.05$; **, $p<0.01$; ****, $p<0.0001$; n.s, not significant.
854
855 **Figure 3. The deletion of *TgCRT* altered microneme secretion, without affecting the microneme**
856 **steady abundance, intracellular trafficking, and intramembrane cleavage on the parasite surface.**
857 **A)** The steady level of micronemal proteins was not altered in the Δ*crt* parasites. Freshly lysed parasites
858 were filter-purified, lysed, and subjected to SDS-PAGE electrophoresis and immunoblotting. The blots
859 were probed with anti-TgMIC2, TgM2AP, and TgMIC5 antibodies, along with anti-TgActin as the loading
860 control. Individual micronemal proteins were normalized against the corresponding TgActin to quantify their
861 steady state expression. **B)** Δ*crt* parasites secreted less micronemal proteins than WT and Δ*crtCRT*
862 parasites, and altered the micronemal secretion patterns. Freshly filter-purified parasites were incubated
863 in medium at 37ºC for 30 min to make constitutive ESAs, or were treated with 1% (v/v) ethanol in medium
864 to produce induced ESAs. The ESA fractions were separated and probed with anti-TgMIC2, TgM2AP, and
865 TgMIC5 antibodies for quantification of the secreted forms of these micronemal proteins. The ESA fractions
866 were also probed with anti-TgGRA7 antibody, a dense granule protein, as the loading control. Statistical
867 significance was determined using unpaired Student's *t*-test. **C)** Pulse invaded and replicated parasites

868 were stained with anti-TgMIC2 and anti-TgM2AP antibodies to examine their intracellular trafficking. No
869 defects were detected in their intracellular trafficking. **D)** Pulse invaded and replicated parasites were also
870 stained with anti-TgROP7 to examine the morphology of the rhoptry and intracellular trafficking of TgROP7.
871 The rhoptry kept similar morphology and trafficking patterns among WT, Δ*crt*, and Δ*crtCRT* strains. The
872 scale bars in the images of pulse invaded and extracellular parasites are 2 μm, and the scale bar in the
873 images of replicated parasites is 5 μm. *, $p<0.05$; **, $p<0.01$; ***, $p<0.001$; ****, $p<0.0001$; n.s., not
874 significant.
875
876 **Figure 4. The transcript and protein levels of a subtilisin-related protease, TgSUB1, were reduced**
877 **in Δ*crt* parasites. A)** The abundance of secreted TgSUB1 in the constitutive and induced ESAs was
878 measured by immunoblotting. There was no detectable TgSUB1 in the constitutive and induced ESAs
879 secreted by Δ*crt* parasites via immunoblotting. **B)** The abundance of plasma membrane-anchored TgSUB1
880 was measured by probing non-permeabilized parasites with antibodies recognizing TgSUB1. The Δ*crt*
881 mutant significantly reduced TgSUB1 on its plasma membrane. **C)** TgSUB1 is a micronemal protein.
882 TgSUB1 and TgMIC5 were both found to localize in the microneme of pulse invaded and replicated WT
883 and Δ*crtCRT* parasites. However, TgSUB1 signal was not detected in the Δ*crt* parasites. **D)** The cell lysates
884 of the Δ*crt* parasites showed that the steady level of TgSUB1 was reduced by ~90% in the Δ*crt* strain. **E)**
885 The transcript level of TgSUB1 was quantified by quantitative PCR. It was also decreased by approximately
886 90% in the Δ*crt* mutant. All assays listed in this figure were replicated at least in triplicate. Statistical
887 significance was calculated using unpaired Student's *t*-test: ***, $p<0.001$; ****, $p<0.0001$; n.s., not
888 significant.
889
890 **Figure 5. The transcript and protein abundances of several VAC-residing proteases were decreased**
891 **in Δ*crt*.**
892 **A)** RNA-Seq was performed in WT and Δ*crt* parasites. Each sample was sequenced in duplicate for
893 statistical comparison. A volcano plot was used to summarize genes that altered their transcription greater
894 than 1.5-fold with statistical significance less than 0.05 in the Δ*crt* mutant relative to the WT strain. Forty-

895 six and fifty-six genes labeled in the blue and red dots became up- and down-regulated in the Δ*crt* mutant,
896 respectively. The blue and red dash lines represented the borderline of 1.5-fold change in gene transcripts,
897 and the genes above the black dash line showed their *p* values of statistical significance below 0.05. **B)**
898 qPCR was used to validate 4 down-regulated proteases that were identified by RNA-Seq analysis, along
899 with two known VAC proteases, TgCPL and TgCPB. *TgAMN*, *TgSCP*, *TgASP1*, and *TgCPB* displayed
900 down-regulated transcription in Δ*crt* parasites compared to WT. **C)** The steady protein abundances of
901 TgCPL and TgCPB were quantified in the lysates of parasites by immunoblotting. The protein levels of
902 TgCPL and TgCPB in Δ*crt* mutant were reduced by ~25% and 60%, respectively, compared to the WT
903 parasites. **D)** TgSCP and TgAMN were endogenously tagged with 3xmyc and 3xHA, respectively, at their
904 C-termini. The expression of the epitope-tagged proteins was confirmed by immunoblotting. The parasites
905 were co-stained with antibodies recognizing their respective epitope tags as well as the VAC and ELC
906 markers. Both TgSCP and TgAMN were localized in the VAC and ELC by immunofluorescence. Statistical
907 significance was performed using unpaired Student's *t*-test. *, $p<0.05$; **, $p<0.01$; n.s., not significant.
908
909 **Figure 6. Suppression of proteolysis in the VAC reduced VAC size and partially restored integrity**
910 **of parasite's endolysosomal system, which recovered TgSUB1 expression, micronemal protein**
911 **trimming in ESAs, and parasite invasion. A)** The Δ*crt* parasites were incubated with 1 μM LHVS, an
912 irreversible inhibitor of TgCPL, for one lytic cycle, followed by a pulse invasion. Parasites were stained with
913 anti-TgCPL antibodies to determine the size of the VAC. The swollen VAC phenotype was significantly
914 reduced in the LHVS-treated parasites. Scale bar = 2μm. **B)** TgCPB, a VAC-residing endo- and exo-
915 peptidase was genetically deleted in the Δ*crt* strain. Schematic illustration for the creation of the Δ*crt*Δ*cpb*
916 mutant. A PCR product carrying a pyrimethamine resistance cassette (DHFR) flanked by 50 bps of the 5'-
917 and 3'-untranscribed regions of *TgCPB* was transfected into WT parasites for double crossover
918 replacement of *TgCPB*. Primers indicated in panel B were used to verify the replacement of *TgCPB* with
919 *DHFR* via PCR and agarose gel electrophoresis. The ablation of *TgCPB* in Δ*crt*Δ*cpb* parasites was also
920 confirmed by immunoblotting. **C)** The sizes of the VAC in WT, Δ*crt*, and Δ*crt*Δ*cpb* parasites were
921 determined by the methods mentioned above. The Δ*crt*Δ*cpb* parasites displayed a partial reduction in the

922 size of the VAC compared to WT parasites. **D)** The pulse invaded parasites showing co-localization
923 between the VAC (TgCPL) and ELC (proTgM2AP) in WT, Δ*crt*, Δ*crtCRT*, and Δ*crt*Δ*cpb* strains were
924 quantified. At least 100 parasites were quantified for each replicate in a total of three replicates. The
925 Δ*crt*Δ*cpb* parasites had a significantly lower percentage of parasites having arrested co-localization
926 between the VAC and ELC compared to the Δ*crt* mutant. **E)** The lysates of WT, Δ*crt*, and Δ*crt*Δ*cpb*
927 parasites were probed with antibodies recognizing TgSUB1.The steady expression of TgSUB1 was
928 restored in Δ*crt*Δ*cpb* parasites. **F)** The constitutive and induced ESAs of WT, Δ*crt*, and Δ*crt*Δ*cpb* strains
929 were made and probed with the antibodies indicated in the figure. The secretion and trimming of
930 micronemal proteins were also recovered in the Δ*crt*Δ*cpb* mutant. **G)** The invasion efficiency of WT, Δ*crt*,
931 and Δ*crt*Δ*cpb* strains was determined using the procedures mentioned above. The Δ*crt*Δ*cpb* parasites
932 showed increased invasion efficiency compared to the Δ*crt* strain, albeit still a lower efficiency than that of
933 WT parasites. Scale bar = 2 µm. Statistical significance was calculated using unpaired Student's *t*-test. *,
934 $p<0.05$; ; **, $p<0.01$; ***, $p<0.001$; n.s., not significant.

935 **Figure 7. TgCRT is a functional transporter and its transport efficiency is correlated with VAC size**
936 **in the parasites. A)** CQ transport by PfCRT and TgCRT (PMA-TgCRT) expressed in *S. cerevisiae*.
937 Transport was extrapolated from CQ-induced growth delays as described in [32,33]. Results are the
938 average of at least four independent experiments ± SEM. EV, empty vector; PfCRT-HB3, wild type PfCRT;
939 PMA-TgCRT, plasma membrane ATPase-TgCRT fusion (see Fig S4); PMA-TgCRT^{T369K}, TgCRT fusion
940 protein harboring T to K substitution at the position analogous to residue 76 in PfCRT (see text). **B)** A
941 mutation of T369K was introduced into WT TgCRT complementation construct by site-directed
942 mutagenesis before it was electroporated into the Δ*crt* mutant. The VAC sizes were determined based on
943 TgCPL staining using the methods mentioned above. The Δ*crt* mutant complemented with TgCRT^{T369K}
944 partially restored its VAC size, but it was still significantly bigger than that transfected with WT TgCRT.
945 Statistical significance was calculated using unpaired Student's *t*-test. *, $p<0.05$; **, $p<0.01$.
946

947 **Figure 8. A model for the regulation of the endolysosomal system in *Toxoplasma* parasites.** The
948 *Toxoplasma* parasite contains a separate endosome-like compartment from the digestive vacuole within

949 its endolysosomal system. When the parasite lacks TgCRT, the VAC gets swollen and cannot separate
950 from its adjacent ELC. This aberrant co-localization leads to reduced transcript and protein abundances of
951 several proteases residing within the endolysosomal system, including TgSUB1. These changes alter the
952 secretion of micronemal proteins, thereby resulting in invasion defects in the TgCRT-null mutant. ELC,
953 endosome-like compartment; ER, endoplasmic reticulum; Go, Golgi apparatus; Mi, microneme; N,
954 nucleus; Rh, rhoptry; TgCRT, *Toxoplasma* chloroquine resistance transporter ortholog; TgSUB1,
955 *Toxoplasma* subtilisin 1; VAC, vacuolar compartment.
956
957 **Table 1. Strains used in this study.**
958
959 **Figure S1. No defects in intramembrane proteolytic cleavage of micronemal protein were observed**
960 **in the Δ*crt* mutant.** Purified, extracellular parasites that had not been permeabilized were stained with
961 anti-TgMIC2 and anti-TgSAG1 antibodies in order to measure the retention of TgMIC2 on the parasite
962 surface. During secretion, the TgMIC2 protein is cleaved by intramembrane rhomboid proteases, such as
963 TgROM4. The abundance of TgMIC2 on the surface of Δ*crt* parasites was similar to that of the WT and
964 Δ*crtCRT* strains, indicating that there is comparable intramembrane cleavage of TgMIC2 among the
965 parasites with or without TgCRT.

966 **Figure S2. Schematic of the endogenous epitope-tagging of *Toxoplasma* putative aminopeptidase**
967 **N (TgAMN, TGGT1_221310) and putative Pro-Xaa serine carboxypeptidase (TgSCP,**
968 **TGGT1_254010). A)** The plasmid encoding Cas9 and sgRNA targeting TgAMN was co-transfected into
969 WT parasites with the PCR product carrying a 3xHA epitope tag and a pyrimethamine resistance cassette
970 (DHFR) flanked by 50 bp regions upstream and downstream of the stop codon of TgAMN. The 3xHA tag
971 and the drug resistance cassette were incorporated at the C-terminus of the *Toxoplasma* putative
972 aminopeptidase N via double crossover homologous recombination mediated by the CRISPR-Cas9
973 genome editing tool. **B)** The putative Pro-Xaa serine carboxypeptidase was endogenously tagged with a
974 3xmyc epitope tag at its C-terminus by single crossover homologous recombination. A 1 kb region
975 upstream of the stop codon of TgSCP was amplified and fused at the 5'-end of the 3xmyc tag to produce

976 the TgSCP-3xmyc tagged plasmid. The 1 kb TgSCP-coding region was cleaved by an endonuclease in
977 the middle prior to transfection to facilitate its integration.
978
979 **Figure S3. The subcellular concave structure in the Δ*crt*Δ*cpb* mutant was shrunken relative to the**
980 **Δ*crt* strain during the extracellular stage.** WT, Δ*crt*, Δ*crtCRT*, and Δ*crt*Δ*cpb* parasites were purified and
981 attached on the surface of a slide for differential interference contrast (DIC) microscopy imaging. Although
982 the Δ*crt*Δ*cpb* mutant still showed an enlarged concave subcellular structure (indicated by the arrow), their
983 sizes were significantly smaller than those in the Δ*crt* mutant. Scale bar = 5 μm.

984 **Figure S4. Alignment of TgCRT and PfCRT primary sequences and schematic of the PMA-TgCRT**
985 **construct expressed in *S. cerevisiae*. A)** Alignment of TgCRT and PfCRT amino acid sequences reveals
986 the 300 most N-terminal residues to be non-homologous, and that they do not encode any putative
987 transmembraneous domains or inter helical loop regions, whereas the remainder of TgCRT is highly
988 homologous to PfCRT. Alignment analysis also revealed that the threonine residue at position 369 within
989 TgCRT corresponds to the well-characterized lysine residue at position 76 within PfCRT (highlighted in
990 red box). Identical and similar residues are highlighted in black and dark grey, respectively. **B)** The 111
991 most N-terminal residues of *S. cerevisiae* plasma membrane ATPase (PMA; black) are fused in frame to
992 the truncated TgCRT (dark grey) from which the first 300 codons have been deleted. The construct
993 includes a C-terminal tag comprised of hexaHIS (H), biotin acceptor domain (B), and V5 epitope tag (V;
994 "HBV" light grey). **C)** Primary amino acid structure of PMA-TgCRT. Residues from PMA are shown in black,
995 those from TgCRT are in shown dark grey, and those comprising the tag are shown in light grey.

996 **Figure S5. Anti-V5 Western blot analysis of TgCRT and PfCRT constructs expressed in *S.***
997 ***cerevisiae*.** Each lane contains 40 μg of protein. Lane 1, yeast membranes for yeast expressing empty
998 vector (EV); lane 2, PfCRT membranes; lane 3, TgCRT membranes; lane 4, PMA-TgCRT fusion
999 membranes; lane 5, blank; lane 6, cytosol from TgCRT yeast; lane 7, cytosol from PMA-TgCRT yeast. The
000 unmodified TgCRT is not expressed in *S. cerevisiae* (lane 3), however, the PMA-TgCRT fusion construct
001 is expressed to similar levels relative to PfCRT [20], and is membrane localized. Lower molecular mass

002 bands in lane 4 are proteolytic products, and can also be found in the cytosolic fraction (lane 7).

003 **Figure S6. Δ*crt* parasites were more sensitive to the treatment of chloroquine than WT parasites.**
004 WT, Δ*crt*, and Δ*crtCRT* parasites expressing luciferase were used to infect host cells in the presence of
005 100 μM or 0 μM chloroquine. The luciferase activity of each strain was measured at 2 and 26 hrs post-
006 infection. The ratios of the luciferase activities determined at 26 hours over that at 2 hrs were plotted.
007 Statistical significance was determined using unpaired Student's *t*-test. *, $p<0.05$; n.s., not significant.

008 **Table S1. Differential gene expression analysis between WT and *Δcrt* strains.** The genes whose
009 fold changes were >1.5 and *p*-values were <0.05 were listed.
010
011 **Table S2. Primers used in this study.**
012
013
014
015

016 **References**

017 1. Laliberté J, Carruthers VB. Host cell manipulation by the human pathogen *Toxoplasma gondii*.
018 Cell Mol Life Sci. 2008;65: 1900–1915. doi:10.1007/s00018-008-7556-x
019 2. Carruthers VB, Tomley FM. Microneme proteins in apicomplexans. Subcell Biochem. 2008;47:
020 33–45.
021 3. Lagal V, Binder EM, Huynh M-H, Kafsack BFC, Harris PK, Diez R, et al. *Toxoplasma gondii*
022 protease TgSUB1 is required for cell surface processing of micronemal adhesive complexes and
023 efficient adhesion of tachyzoites. Cell Microbiol. 2010;12: 1792–1808. doi:10.1111/j.1462-
024 5822.2010.01509.x
025 4. Parussini F, Coppens I, Shah PP, Diamond SL, Carruthers VB. Cathepsin L occupies a vacuolar
026 compartment and is a protein maturase within the endo/exocytic system of *Toxoplasma gondii*.
027 Mol Microbiol. 2010;76: 1340–1357. doi:10.1111/j.1365-2958.2010.07181.x
028 5. Dogga SK, Mukherjee B, Jacot D, Kockmann T, Molino L, Hammoudi P-M, et al. A druggable
029 secretory protein maturase of *Toxoplasma* essential for invasion and egress. Elife. 2017;6: 223.
030 doi:10.7554/eLife.27480
031 6. Buguliskis JS, Brossier F, Shuman J, Sibley LD. Rhomboid 4 (ROM4) affects the processing of
032 surface adhesins and facilitates host cell invasion by *Toxoplasma gondii.* PLoS Pathog. 2010;6:
033 e1000858. doi:10.1371/journal.ppat.1000858
034 7. Santos JM, Ferguson DJP, Blackman MJ, Soldati-Favre D. Intramembrane cleavage of AMA1
035 triggers *Toxoplasma* to switch from an invasive to a replicative mode. Science. 2011;331: 473–
036 477. doi:10.1126/science.1199284
037 8. Parussini F, Tang Q, Moin SM, Mital J, Urban S, Ward GE. Intramembrane proteolysis of
038 *Toxoplasma* apical membrane antigen 1 facilitates host-cell invasion but is dispensable for
039 replication. Proc Natl Acad Sci USA. 2012;109: 7463–7468. doi:10.1073/pnas.1114661109
040 9. Dou Z, Carruthers VB. Cathepsin proteases in *Toxoplasma gondii*. Adv Exp Med Biol. Boston, MA:
041 Springer US; 2011;712: 49–61. doi:10.1007/978-1-4419-8414-2_4

042 10. Dou Z, McGovern OL, Di Cristina M, Carruthers VB. *Toxoplasma gondii* ingests and digests host
043 cytosolic proteins. MBio. 2014;5: e01188–14. doi:10.1128/mBio.01188-14
044 11. Miller SA, Binder EM, Blackman MJ, Carruthers VB, Kim K. A conserved subtilisin-like protein
045 TgSUB1 in microneme organelles of *Toxoplasma gondii*. J Biol Chem. 2001;276: 45341–45348.
046 doi:10.1074/jbc.M106665200
047 12. Di Cristina M, Dou Z, Lunghi M, Kannan G, Huynh M-H, McGovern OL, et al. *Toxoplasma*
048 depends on lysosomal consumption of autophagosomes for persistent infection. Nat Microbiol.
049 2017;2: 17096. doi:10.1038/nmicrobiol.2017.96
050 13. Dou Z, Coppens I, Carruthers VB. Non-canonical maturation of two papain-family proteases in
051 *Toxoplasma gondii*. J Biol Chem. 2013;288: 3523–3534. doi:10.1074/jbc.M112.443697
052 14. Warring SD, Dou Z, Carruthers VB, McFadden GI, van Dooren GG. Characterization of the
053 chloroquine resistance transporter homologue in *Toxoplasma gondii*. Euk Cell. 2014;13: 1360–
054 1370. doi:10.1128/EC.00027-14
055 15. Liu J, Pace D, Dou Z, King TP, Guidot D, Li Z-H, et al. A vacuolar-H^+-pyrophosphatase (TgVP1) is
056 required for microneme secretion, host cell invasion, and extracellular survival of *Toxoplasma*
057 *gondii*. Mol Microbiol. 2014;93: 698–712. doi:10.1111/mmi.12685
058 16. Gligorijevic B, Bennett T, McAllister R, Urbach JS, Roepe PD. Spinning disk confocal microscopy
059 of live, intraerythrocytic malarial parasites. 2. Altered vacuolar volume regulation in drug resistant
060 malaria. Biochemistry. 2006;45: 12411–12423. doi:10.1021/bi0610348
061 17. Lee AH, Dhingra SK, Lewis IA, Singh MK, Siriwardana A, Dalal S, et al. Evidence for Regulation of
062 Hemoglobin Metabolism and Intracellular Ionic Flux by the *Plasmodium falciparum* Chloroquine
063 Resistance Transporter. Sci Rep. 2018;8: 13578. doi:10.1038/s41598-018-31715-9
064 18. Paguio MF, Cabrera M, Roepe PD. Chloroquine transport in *Plasmodium falciparum.* 2. Analysis
065 of PfCRT-mediated drug transport using proteoliposomes and a fluorescent chloroquine probe.
066 Biochemistry. 2009;48: 9482–9491. doi:10.1021/bi901035j

067 19. Juge N, Moriyama S, Miyaji T, Kawakami M, Iwai H, Fukui T, et al. *Plasmodium falciparum*
068 chloroquine resistance transporter is a H^+-coupled polyspecific nutrient and drug exporter. Proc
069 Natl Acad Sci USA. 2015;112: 3356–3361. doi:10.1073/pnas.1417102112
070 20. Callaghan PS, Hassett MR, Roepe PD. Functional Comparison of 45 Naturally Occurring Isoforms
071 of the *Plasmodium falciparum* Chloroquine Resistance Transporter (PfCRT). Biochemistry.
072 2015;54: 5083–5094. doi:10.1021/acs.biochem.5b00412
073 21. Waller KL, Muhle RA, Ursos LM, Horrocks P, Verdier-Pinard D, Sidhu ABS, et al. Chloroquine
074 resistance modulated in vitro by expression levels of the *Plasmodium falciparum* chloroquine
075 resistance transporter. J Biol Chem. 2003;278: 33593–33601. doi:10.1074/jbc.M302215200
076 22. Huynh M-H, Carruthers VB. Tagging of endogenous genes in a *Toxoplasma gondii* strain lacking
077 Ku80. Euk Cell. 2009;8: 530–539. doi:10.1128/EC.00358-08
078 23. Larson ET, Parussini F, Huynh M-H, Giebel JD, Kelley AM, Zhang L, et al. *Toxoplasma gondii*
079 cathepsin L is the primary target of the invasion-inhibitory compound morpholinurea-leucyl-
080 homophenyl-vinyl sulfone phenyl. J Biol Chem. 2009;284: 26839–26850.
081 doi:10.1074/jbc.M109.003780
082 24. McGovern OL, Rivera-Cuevas Y, Kannan G, Narwold AJ, Carruthers VB. Intersection of endocytic
083 and exocytic systems in *Toxoplasma gondii*. Traffic. 2018;19: 336–353. doi:10.1111/tra.12556
084 25. Blader IJ, Coleman BI, Chen C-T, Gubbels M-J. Lytic Cycle of Toxoplasma gondii: 15 Years Later.
085 Annu Rev Microbiol. 2015;69: 463–485. doi:10.1146/annurev-micro-091014-104100
086 26. Hager KM, Carruthers VB. MARveling at parasite invasion. Trends Parasitol. 2008;24: 51–54.
087 doi:10.1016/j.pt.2007.10.008
088 27. Dubremetz J-F. Rhoptries are major players in *Toxoplasma gondii* invasion and host cell
089 interaction. Cell Microbiol. 2007;9: 841–848. doi:10.1111/j.1462-5822.2007.00909.x
090 28. Shen B, Buguliskis JS, Lee TD, Sibley LD. Functional analysis of rhomboid proteases during
091 Toxoplasma invasion. MBio. 2014;5: e01795–14. doi:10.1128/mBio.01795-14
092 29. Sloves P-J, Delhaye S, Mouveaux T, Werkmeister E, Slomianny C, Hovasse A, et al. *Toxoplasma*
093 Sortilin-like Receptor Regulates Protein Transport and Is Essential for Apical Secretory Organelle

094 Biogenesis and Host Infection. Cell Host Microbe. 2012;11: 515–527.
095 doi:10.1016/j.chom.2012.03.006
096 30. Saouros S, Dou Z, Marchant J, Carruthers VB, Matthews S. Microneme protein 5 regulates the
097 activity of *Toxoplasma* subtilisin 1 by mimicking a subtilisin prodomain. J Biol Chem. 2012;287:
098 36029–36040. doi:10.1074/jbc.M112.389825
099 31. Zhang H, Howard EM, Roepe PD. Analysis of the antimalarial drug resistance protein Pfcrt
100 expressed in yeast. J Biol Chem. 2002;277: 49767–49775. doi:10.1074/jbc.M204005200
101 32. Baro NK, Pooput C, Roepe PD. Analysis of chloroquine resistance transporter (CRT) isoforms and
102 orthologues in *S. cerevisiae* yeast. Biochemistry. 2011;50: 6701–6710. doi:10.1021/bi200922g
103 33. Baro NK, Callaghan PS, Roepe PD. Function of resistance conferring *Plasmodium falciparum*
104 chloroquine resistance transporter isoforms. Biochemistry. 2013;52: 4242–4249.
105 doi:10.1021/bi400557x
106 34. Sidhu ABS, Verdier-Pinard D, Fidock DA. Chloroquine resistance in *Plasmodium falciparum*
107 malaria parasites conferred by pfcrt mutations. Science. 2002;298: 210–213.
108 doi:10.1126/science.1074045
109 35. Martin RE, Marchetti RV, Cowan AI, Howitt SM, Bröer S, Kirk K. Chloroquine transport via the
110 malaria parasite's chloroquine resistance transporter. Science. 2009;325: 1680–1682.
111 doi:10.1126/science.1175667
112 36. Binder EM, Lagal V, Kim K. The Prodomain of T*oxoplasma gondii* GPI-Anchored Subtilase
113 TgSUB1 Mediates its Targeting to Micronemes. Traffic. 2008;9: 1485–1496. doi:10.1111/j.1600-
114 0854.2008.00774.x
115 37. Settembre C, Di Malta C, Polito VA, Garcia Arencibia M, Vetrini F, Erdin S, et al. TFEB links
116 autophagy to lysosomal biogenesis. Science. 2011;332: 1429–1433.
117 doi:10.1126/science.1204592
118 38. Fu M, Blackshear PJ. RNA-binding proteins in immune regulation: a focus on CCCH zinc finger
119 proteins. Nat Rev Immunol. 2017;17: 130–143. doi:10.1038/nri.2016.129

120 39. Carballo E, Lai WS, Blackshear PJ. Feedback Inhibition of Macrophage Tumor Necrosis Factor-α
121 Production by Tristetraprolin. Science. 1998;281: 1001–1005. doi:10.1126/science.281.5379.1001
122 40. Lewis IA, Wacker M, Olszewski KL, Cobbold SA, Baska KS, Tan A, et al. Metabolic QTL analysis
123 links chloroquine resistance in *Plasmodium falciparum* to impaired hemoglobin catabolism.
124 Neafsey DE, editor. PLoS Genet. 2014;10: e1004085. doi:10.1371/journal.pgen.1004085
125 41. Sijwali PS, Rosenthal PJ. Gene disruption confirms a critical role for the cysteine protease
126 falcipain-2 in hemoglobin hydrolysis by *Plasmodium falciparum*. Proc Natl Acad Sci USA.
127 2004;101: 4384–4389. doi:10.1073/pnas.0307720101
128 42. Miranda K, Pace DA, Cintron R, Rodrigues JCF, Fang J, Smith A, et al. Characterization of a
129 novel organelle in *Toxoplasma gondii* with similar composition and function to the plant vacuole.
130 Mol Microbiol. 2010;76: 1358–1375. doi:10.1111/j.1365-2958.2010.07165.x
131 43. Warmka J, Hanneman J, Lee J, Amin D, Ota I. Ptc1, a type 2C Ser/Thr phosphatase, inactivates
132 the HOG pathway by dephosphorylating the mitogen-activated protein kinase Hog1. Mol Cell Biol.
133 2001;21: 51–60. doi:10.1128/MCB.21.1.51-60.2001
134 44. Mapes J, Ota IM. Nbp2 targets the Ptc1-type 2C Ser/Thr phosphatase to the HOG MAPK
135 pathway. EMBO J. 2004;23: 302–311. doi:10.1038/sj.emboj.7600036
136 45. González A, Ruiz A, Serrano R, Ariño J, Casamayor A. Transcriptional profiling of the protein
137 phosphatase 2C family in yeast provides insights into the unique functional roles of Ptc1. J Biol
138 Chem. 2006;281: 35057–35069. doi:10.1074/jbc.M607919200
139 46. Shen B, Brown KM, Lee TD, Sibley LD. Efficient Gene Disruption in Diverse Strains of
140 *Toxoplasma gondii* Using CRISPR/CAS9. MBio. 2014;5: e01114–14. doi:10.1128/mBio.01114-14
141 47. Sidik SM, Hackett CG, Tran F, Westwood NJ, Lourido S. Efficient Genome Engineering of
142 Toxoplasma gondii Using CRISPR/Cas9. Blader IJ, editor. PLoS ONE. 2014;9: e100450–8.
143 doi:10.1371/journal.pone.0100450
144 48. Kaja S, Payne AJ, Singh T, Ghuman JK, Sieck EG, Koulen P. An optimized lactate
145 dehydrogenase release assay for screening of drug candidates in neuroscience. Journal of
146 Pharmacol Toxicol Methods. 2015;73: 1–6. doi:10.1016/j.vascn.2015.02.001

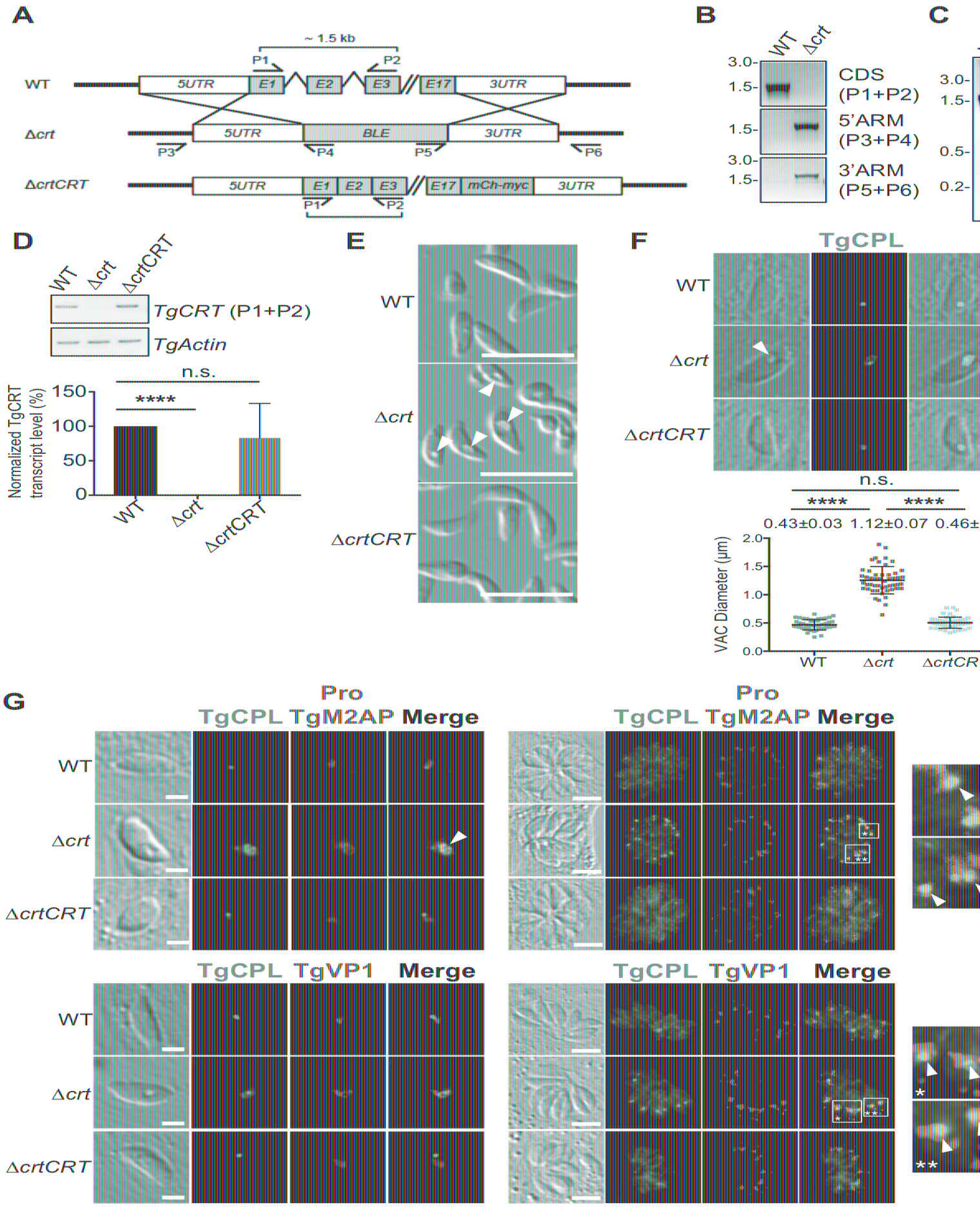
A
~ 1.5 kb
P1
P2
WT
5UTR
E1
E2
E3
E17
3UTR
Δcrt
BLE
P3
P4
P5
P6
ΔcrtCRT
mCh-myc
B
WT
Δcrt
CDS (P1+P2)
5'ARM (P3+P4)
3'ARM (P5+P6)
C
D
TgCRT (P1+P2)
TgActin
n.s.
****
Normalized TgCRT transcript level (%)
E
F
TgCPL
0.43±0.03
1.12±0.07
VAC Diameter (μm)
G
Pro
TgCPL TgM2AP Merge
TgCPL TgVP1 Merge

Figure 1

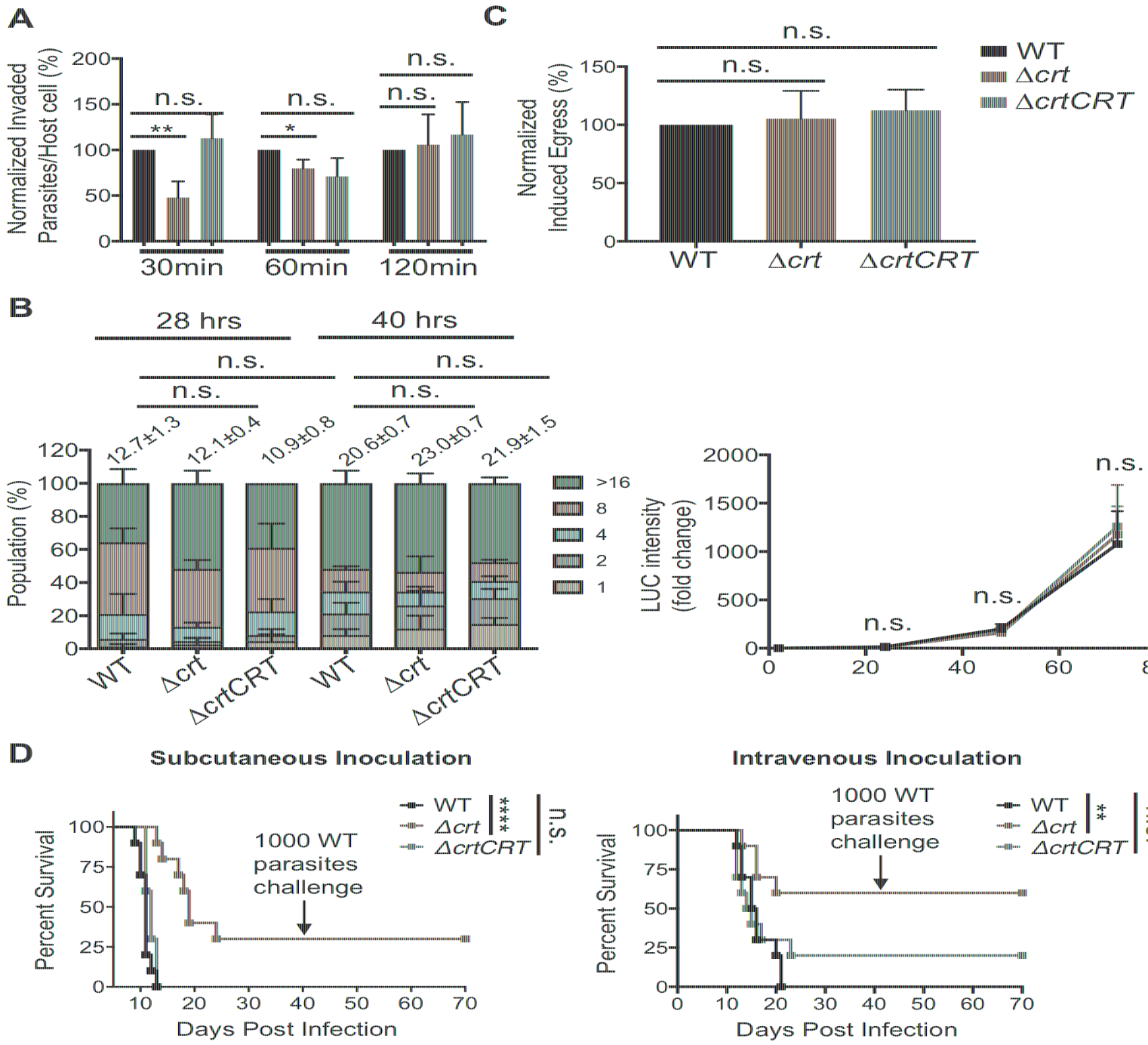
A
Normalized Invaded Parasites/Host cell (%)
200
150
100
50
0
n.s.
**
n.s.
*
n.s.
n.s.
30min
60min
120min
C
Normalized Induced Egress (%)
150
100
50
0
n.s.
n.s.
WT
Δcrt
ΔcrtCRT
B
28 hrs
40 hrs
n.s.
n.s.
n.s.
n.s.
12.7±1.3
12.1±0.4
10.9±0.8
20.6±0.7
23.0±0.7
21.9±1.5
Population (%)
120
100
80
60
40
20
0
>16
8
4
2
1
LUC intensity (fold change)
2000
1500
1000
500
0
n.s.
n.s.
n.s.
0
20
40
60
D
Subcutaneous Inoculation
Intravenous Inoculation
Percent Survival
100
75
50
25
0
1000 WT parasites challenge
WT
Δcrt
ΔcrtCRT
****
n.s.
**
10
20
30
40
50
60
70
Days Post Infection

Figure 2

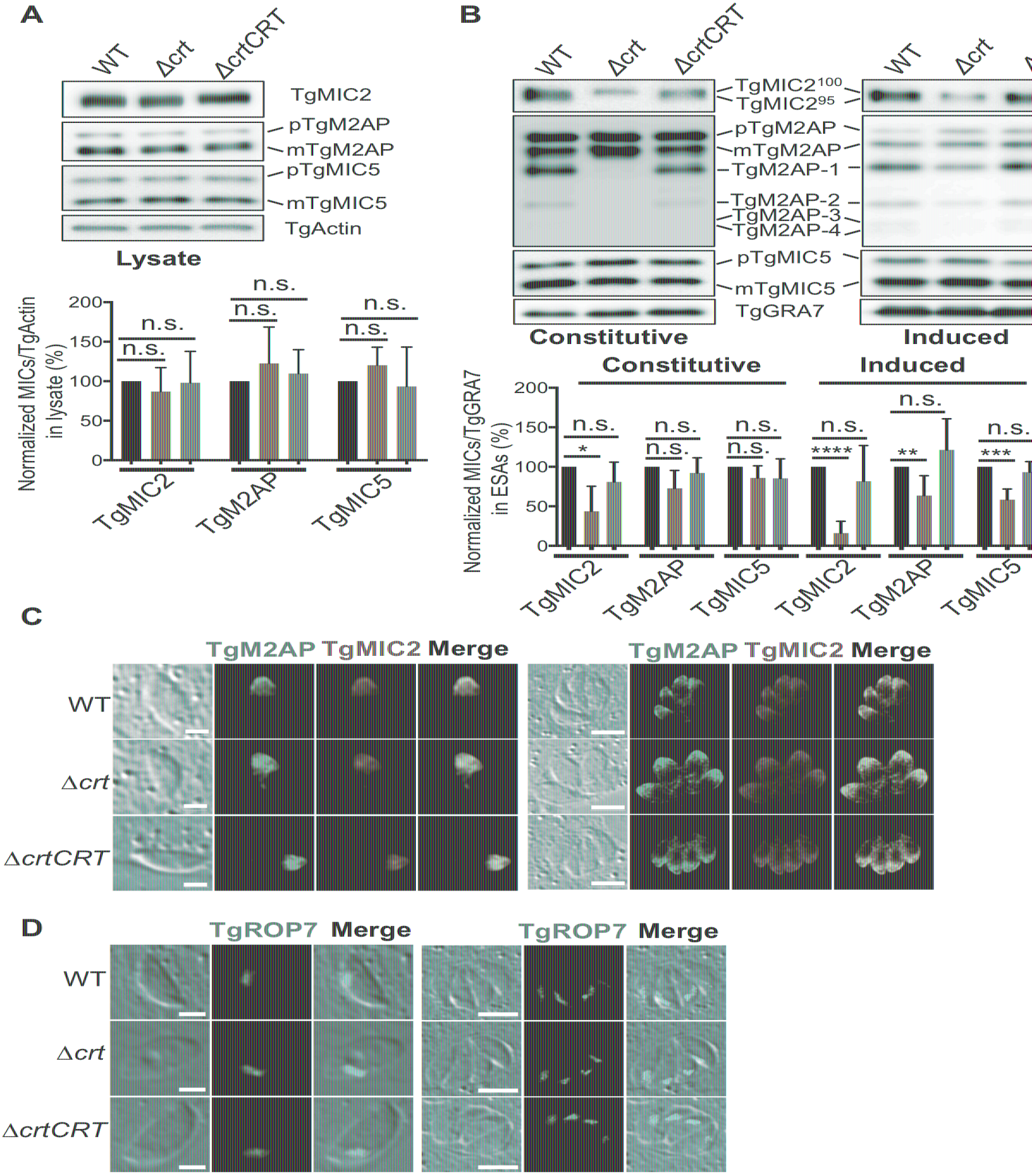
A
WT
Δcrt
ΔcrtCRT
TgMIC2
pTgM2AP
mTgM2AP
pTgMIC5
mTgMIC5
TgActin
Lysate
Normalized MICs/TgActin in lysate (%)
200
150
100
50
0
n.s.
TgMIC2
TgM2AP
TgMIC5
B
TgMIC2100
TgMIC295
pTgM2AP
mTgM2AP
TgM2AP-1
TgM2AP-2
TgM2AP-3
TgM2AP-4
pTgMIC5
mTgMIC5
TgGRA7
Constitutive
Induced
Normalized MICs/TgGRA7 in ESAs (%)
*
****
**
***
C
TgM2AP TgMIC2 Merge
WT
Δcrt
ΔcrtCRT
D
TgROP7 Merge

Figure 3

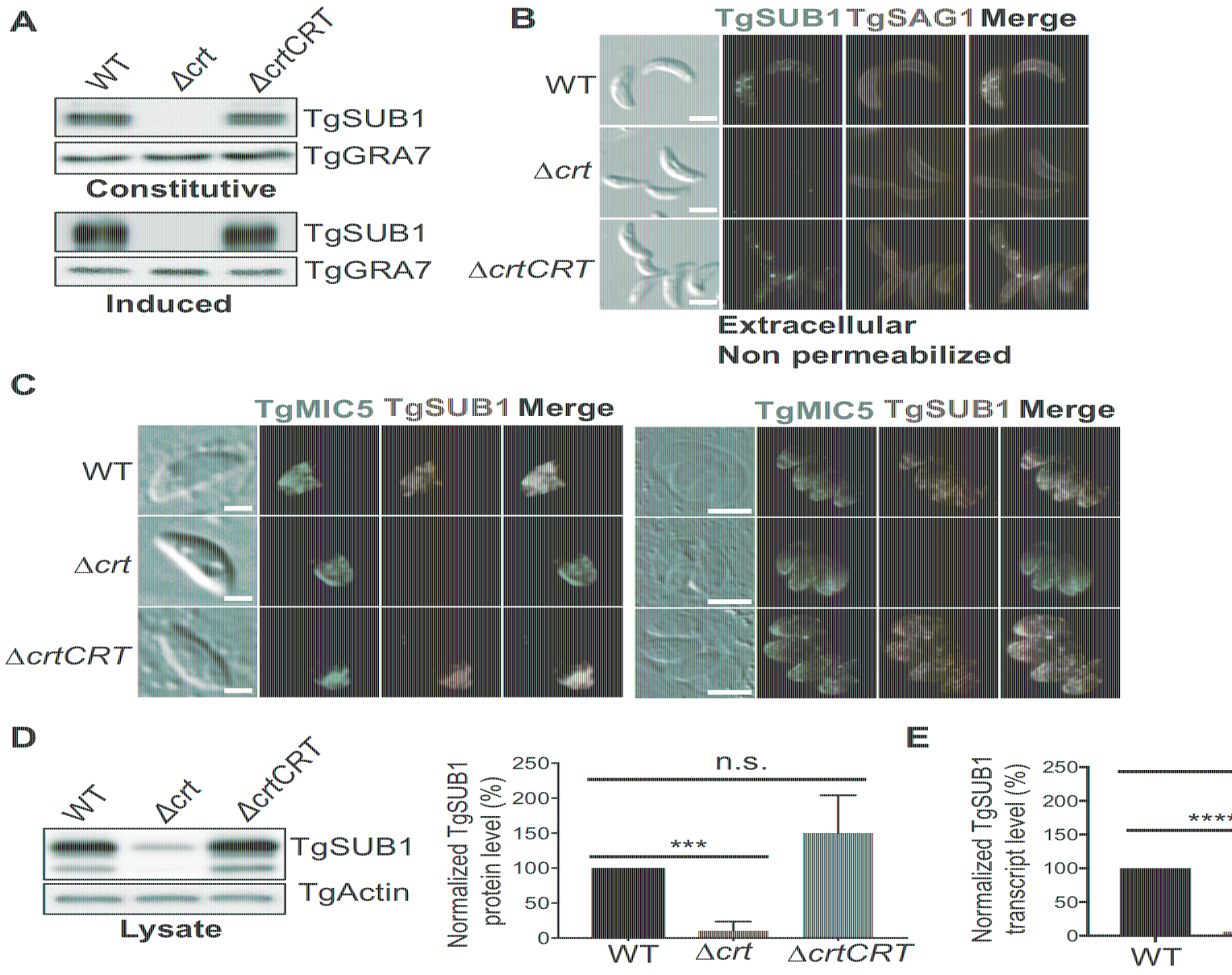
A
WT
Δcrt
ΔcrtCRT
TgSUB1
TgGRA7
Constitutive
TgSUB1
TgGRA7
Induced
B
TgSUB1 TgSAG1 Merge
WT
Δcrt
ΔcrtCRT
Extracellular
Non permeabilized
C
TgMIC5 TgSUB1 Merge
TgMIC5 TgSUB1 Merge
WT
Δcrt
ΔcrtCRT
D
WT
Δcrt
ΔcrtCRT
TgSUB1
TgActin
Lysate
Normalized TgSUB1 protein level (%)
250
200
150
100
50
0
n.s.
***
WT
Δcrt
ΔcrtCRT
E
Normalized TgSUB1 transcript level (%)
250
200
150
100
50
0
WT

Figure 4

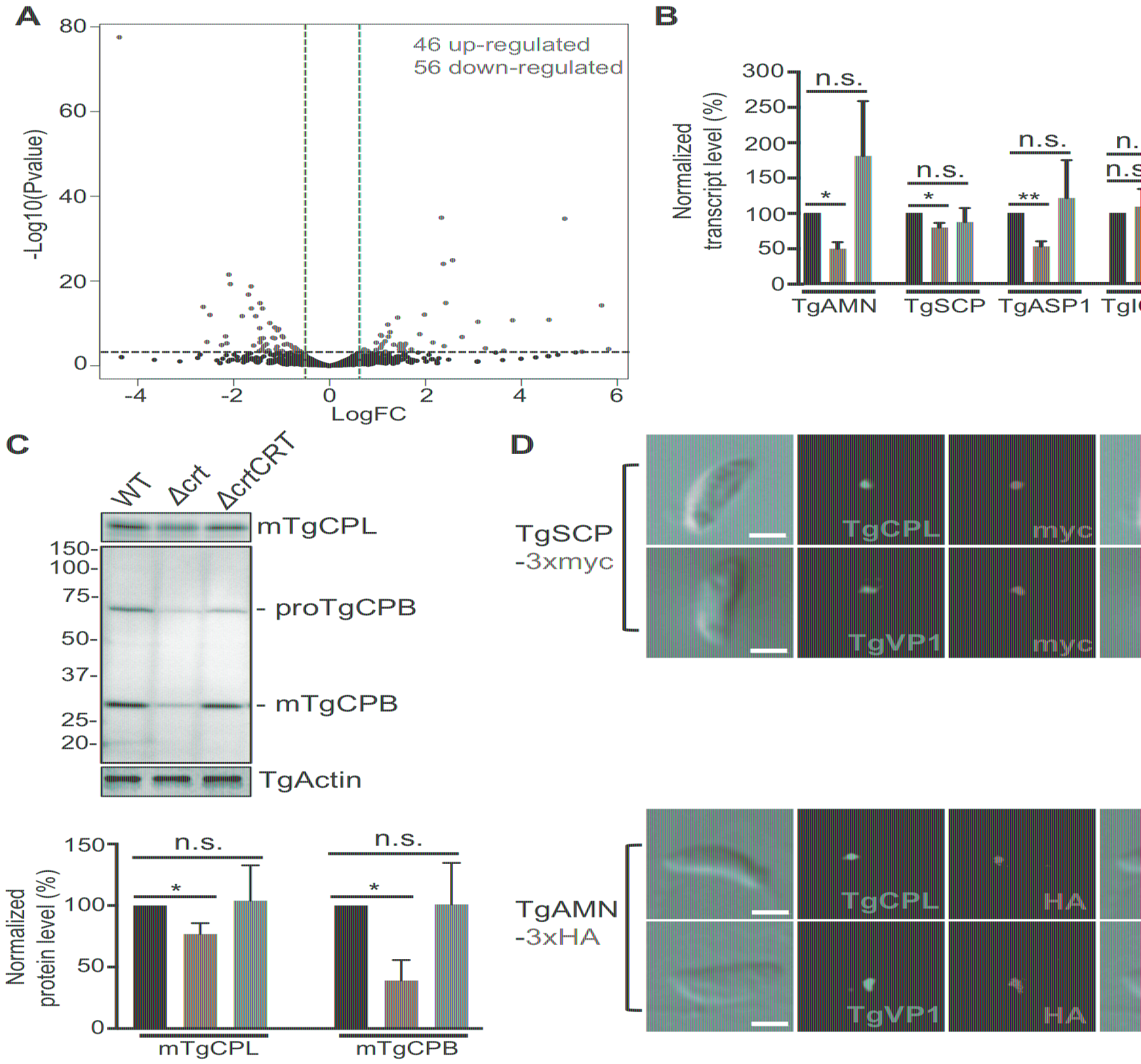
A
46 up-regulated
56 down-regulated
-Log10(Pvalue)
LogFC
B
Normalized transcript level (%)
n.s.
*
**
TgAMN
TgSCP
TgASP1
C
WT
Δcrt
ΔcrtCRT
mTgCPL
proTgCPB
mTgCPB
TgActin
Normalized protein level (%)
mTgCPL
mTgCPB
D
TgSCP
-3xmyc
TgCPL
TgVP1
myc
TgAMN
-3xHA
HA

Figure 5

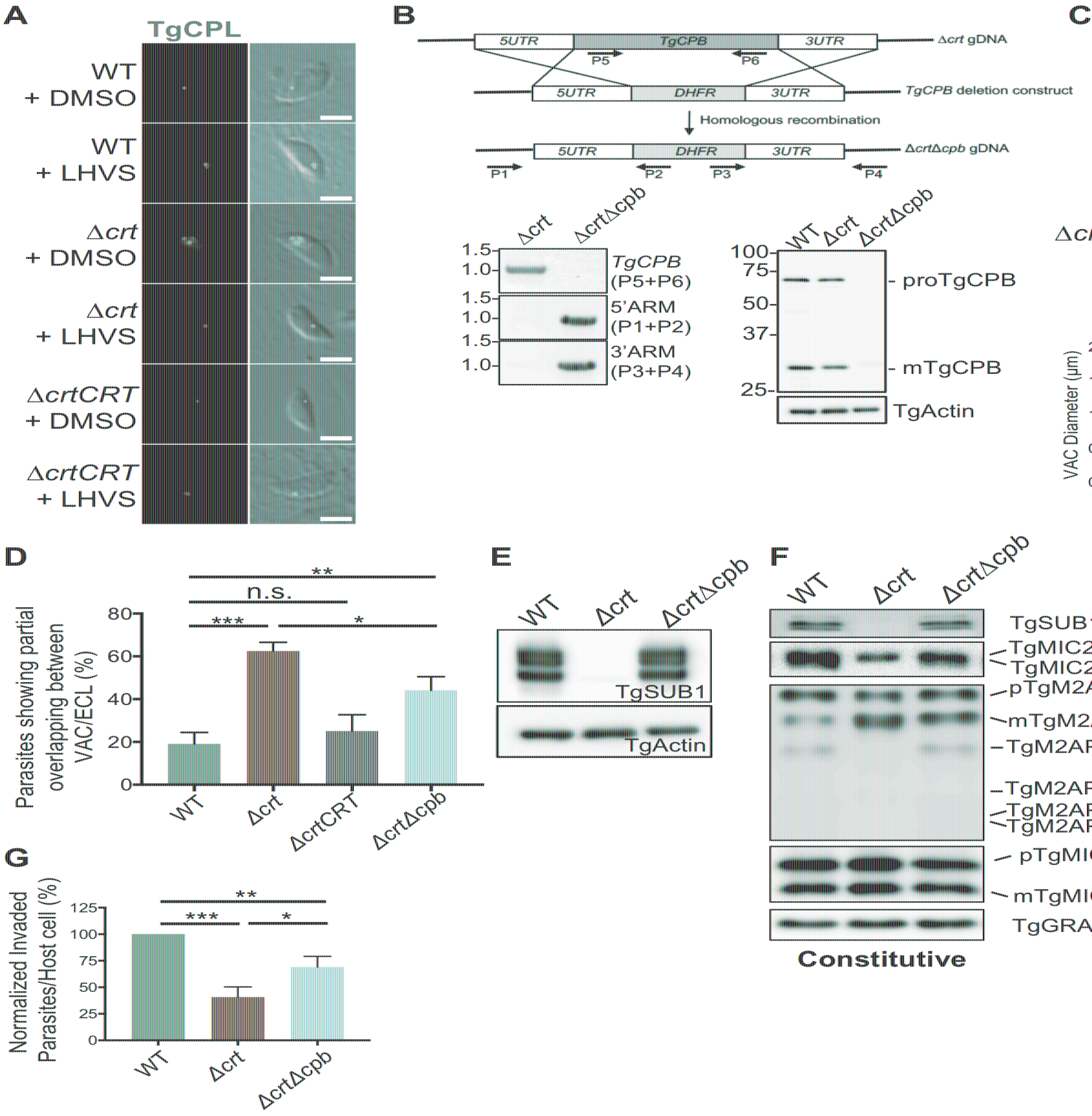
A
TgCPL
WT + DMSO
WT + LHVS
Δcrt + DMSO
Δcrt + LHVS
ΔcrtCRT + DMSO
ΔcrtCRT + LHVS
B
5UTR
TgCPB
3UTR
Δcrt gDNA
P5
P6
5UTR
DHFR
3UTR
TgCPB deletion construct
Homologous recombination
5UTR
DHFR
3UTR
ΔcrtΔcpb gDNA
P1
P2
P3
P4
Δcrt
ΔcrtΔcpb
TgCPB (P5+P6)
5'ARM (P1+P2)
3'ARM (P3+P4)
WT
Δcrt
ΔcrtΔcpb
proTgCPB
mTgCPB
TgActin
C
VAC Diameter (μm)
D
Parasites showing partial overlapping between VAC/ECL (%)
n.s.
**
***
*
WT
Δcrt
ΔcrtCRT
ΔcrtΔcpb
E
WT
Δcrt
ΔcrtΔcpb
TgSUB1
TgActin
F
WT
Δcrt
ΔcrtΔcpb
TgSUB1
TgMIC2
TgMIC2
pTgM2A
mTgM2
TgM2AP
TgM2AP
TgM2AP
TgM2AP
pTgMIC
mTgMIC
TgGRA
Constitutive
G
Normalized Invaded Parasites/Host cell (%)
**
***
*
WT
Δcrt
ΔcrtΔcpb

Figure 6

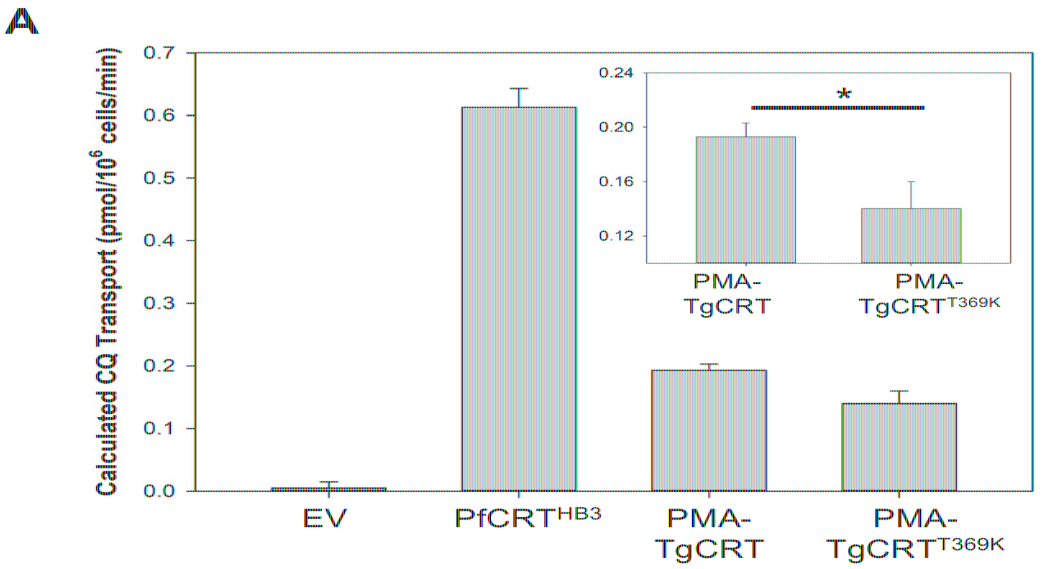
A
Calculated CQ Transport (pmol/10^6 cells/min)
0.7
0.6
0.5
0.4
0.3
0.2
0.1
0.0
EV
PfCRTHB3
PMA-TgCRT
PMA-TgCRTT369K
0.24
0.20
0.16
0.12
*
PMA-TgCRT
PMA-TgCRTT369K

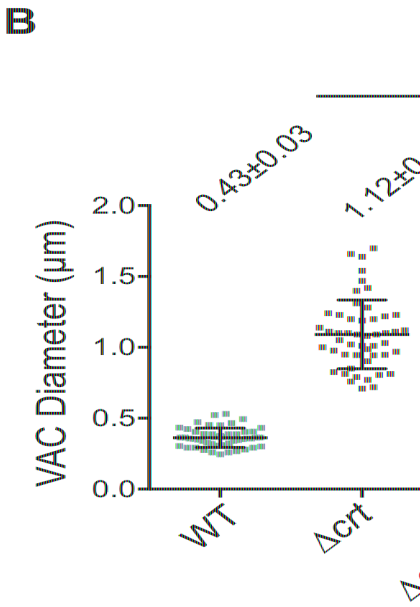
B
VAC Diameter (µm)
2.0
1.5
1.0
0.5
0.0
0.43±0.03
1.12±0
WT
Δcrt

Figure 7

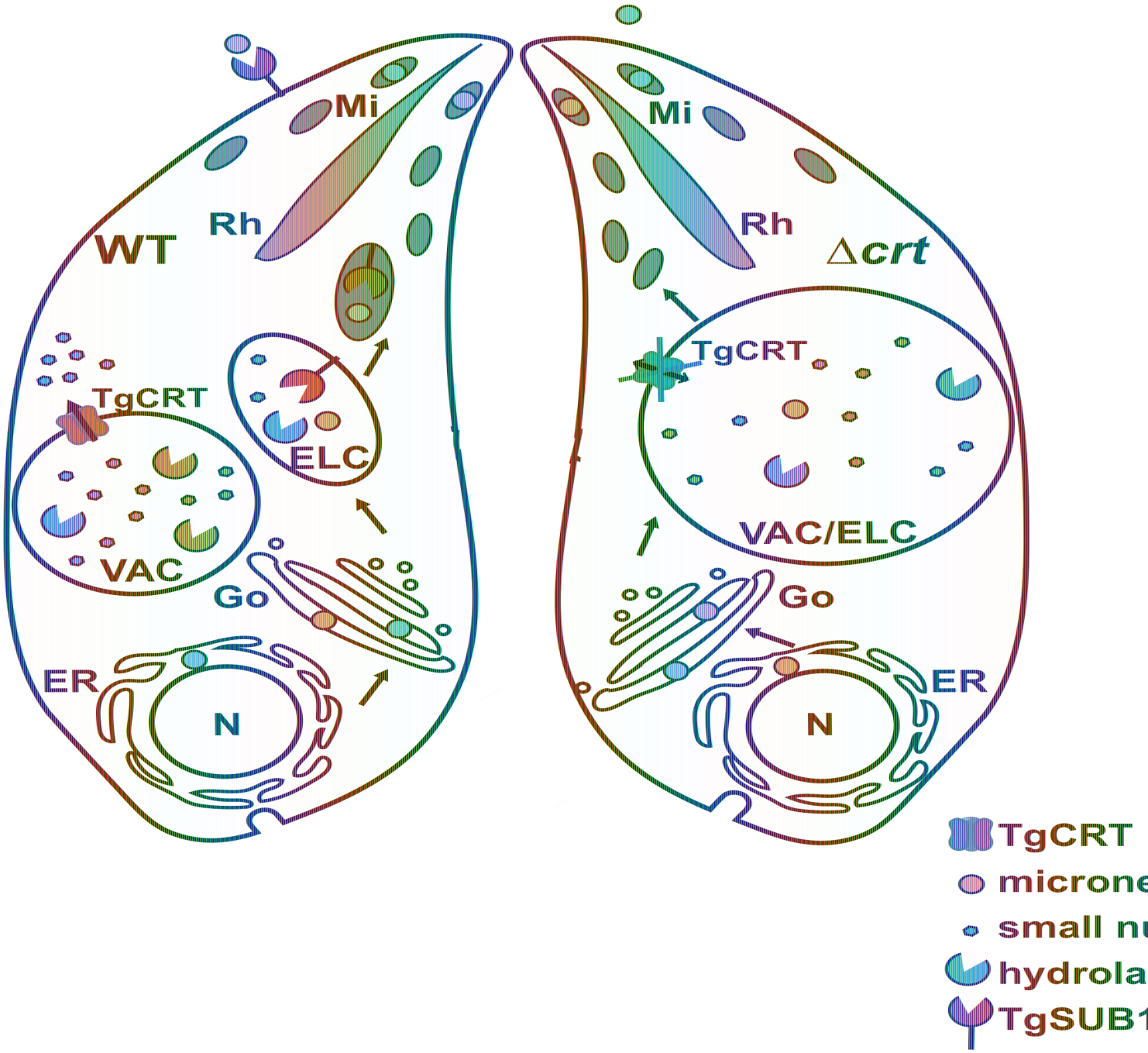
WT
Mi
Rh
TgCRT
ELC
VAC
Go
ER
N
Δcrt
Mi
Rh
TgCRT
VAC/ELC
Go
ER
N
TgCRT
microne
small nu
hydrola
TgSUB1

Figure 8